UNITED NATIONS UNIVERSITY
GEOTHERMAL TRAINING PROGRAMME
Orkustofnun, Grensasvegur 9,
IS-108 Reykjavik, Iceland

Reports 2013
Number 19

1D JOINT INVERSION OF TEM AND MT DATA: SUSWA GEOTHERMAL FIELD, RIFT VALLEY, KENYA

Yussuf N. Mohamud
Geothermal Development Company, Ltd. – GDC
P.O. Box 17700 – 2010
Nakuru
KENYA
ynoor@gdc.co.ke

ABSTRACT

Suswa geothermal prospect is the southernmost trachyte shield volcanic complex at the base of the Kenyan Rift floor. It is located about 15 and 30 km to the south of Mt. Longonot and Olkaria Domes, respectively, and is characterized by 2 nested calderas. The last volcanic activity in the area occurred less than 400 years ago in the inner caldera. Geothermal surface indicators are in the form of fumaroles, alterations, young lavas and geothermal grass. Unique to Mt. Suswa among the volcanic complexes in the rift axis is its phonolitic composition in addition to trachyte and pyroclastic formations. The main structures in the area trend N-S, ENE-WSW and along the caldera ring structures. The main recharge is from the rift flanks to the east and west of the prospect area.

The result from resistivity surveys using 1D joint inversion of MT and TEM data indicates the presence of a deep conductor at 4000 m b.s.l. in the Kisharo area, a dominant resistive structure at sea level (0 m) and a conductive layer between 1000 m a.s.l. and 1500 m a.s.l. The deep conductor below the caldera could be the heat source of the prospect. A profile (profile 2) across the southern slopes of Mt. Suswa reveals a deep lying conductor in pockets between 7500 and 3000 m b.s.l., while above 0 m, near parallel conductive layers are prominent.

In the Kisharo area at the floor of the outer caldera, with intense fumarolic activities, the resistivity is high near the surface, probably due to dry steam associated with a deep groundwater table.

1. INTRODUCTION

Suswa geothermal prospect is located in the southern part of the Kenyan Great Rift floor in a chain of geothermal prospects along major tectonic structures extending from Lake Turkana in the north to Lake Magadi in the south (Figure 1). At the southernmost exit of the volcanic shield complex is Mt. Suswa, a large trachytic shield volcano with two nested summit calderas that erupted trachyte, phonolite lavas and tuffs from 240 to >100 ka (White et al., 2012). The inner caldera is composed of an annular ring, and a central resurgence block (island block) which formed as a result of uplift. It is about 4 km in diameter. The outer caldera measures 12 by 10 km, oriented ENE-WSW (Lagat, 2003). The prospect area extends more than 700 km^2 and stands 800 m above the rift floor with the highest elevation point

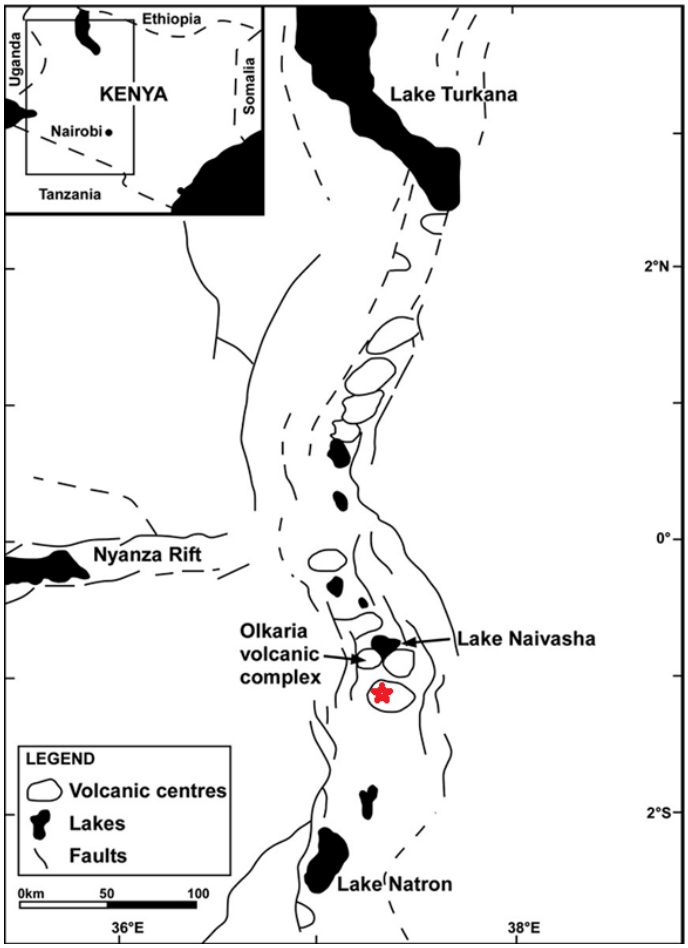

FIGURE 1: Map of the Kenya Rift faults showing the major Quaternary central volcanoes and the location of the Suswa volcanic shield complex (red star) (modified from Karingithi et al., 2010)

of 2356 m above sea level. The annular ring is phonolitic in composition and it is where the latest volcanic activity took place less than 400 years before the present (BP) (GDC, 2013).

The presence of young lava and fumaroles indicates a thermally active surface at depth. McCall and Bristow (1965) attributed extensive fumarolic activity in Suswa at the present time to emitted steam, probably derived from meteoric water but charged with CO_2 and probably nitrogen. The manifestations are found within the outer caldera floor, caldera walls and on the slopes of the volcano, especially the southern slopes in Soitamurt where they occur in the form of altered grounds, steaming grounds and fumaroles. The hottest fumarolic activities occur along the wall of the inner caldera (GDC, 2013).

Surface studies by Omenda (1997), Geothermal Development Company in 2013 and KenGen in 1993-94 all indicated possibilities of a high-temperature field in Suswa despite the fact that no exploration wells have yet been drilled in the area.

Geophysical methods as part of geoscientific exploration techniques are the key to geothermal resource assessment before drilling. In Suswa, MT and TEM resistivity survey methods were used due to their direct relationship to the properties of the subsurface that characterize a geothermal reservoir such as salinity, temperature, permeability, porosity, water rock interaction and alteration (Hersir and Björnsson, 1991).

The main objective of this work is to process the data collected in Suswa using magnetotelluric (MT) and transient electromagnetic methods (TEM), 1D joint inversion of TEM data and statically shift corrected MT data, and to generate iso-depth maps and cross-sections using *TemX* and *TEMTD* Linux based programs developed at Iceland GeoSurvey (ISOR) by Árnason (2006a and 2006b).

2. RESISTIVITY OF ROCKS

Electrical resistivity is the most powerful geophysical method in geothermal prospecting and uses the basic Ohm´s law in detecting geothermal signatures in subsurface rocks. The common principle of all electric methods is to induce currents into the ground and monitor the signal generated at the surface by current distribution (Hersir and Björnsson, 1991). These are detected because of resistivity contrasts caused by several factors in the otherwise resistive rock. Geothermal fluids, altered rocks, recharge conduits and heat sources are all characterized by low resistivity. However, since apparent resistivity is measured, it needs to be transformed into specific resistivity which depends on the material.

The specific resistivity, ρ, defined through Ohm´s law, states that the electrical field strength $\boldsymbol{E}$ (V/m) at a point in a material is proportional to the current density, $\boldsymbol{j}$ (A/m^2):

$$\boldsymbol{E} = \rho \boldsymbol{j} \tag{1}$$

Resistivity ρ (Ωm) is also defined as the ratio of potential difference ΔV (V) to the current I (A) across a material with a cross-sectional area of 1 m^2 which is 1 m long:

$$\rho = \Delta V / I \tag{2}$$

Solid rocks are natural insulators unless their properties are altered to a porous media by geophysical or geochemical processes, thereby increasing their conductivity level. The main determinants of rock conductivity near earth surfaces are porosity and conductivity of fluid, dependent on salinity and temperature which changes with depth and region (Vozoff, 1990). Additionally, the type of fluid and saturation level, degree of alteration and mineral assemblages further affect the conductivity of a porous rock. The conduction mechanisms in a geothermal system are due to free ions and fluids in the porous rock and electrons in minerals at the water-rock interface (Flóvenz et al., 2012).

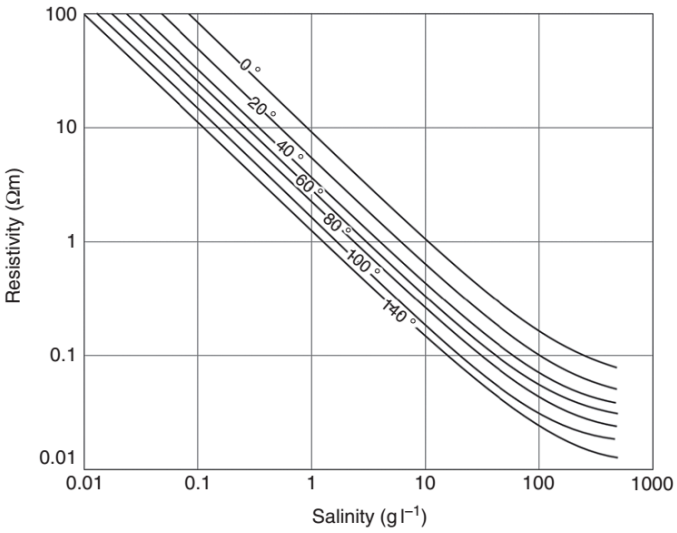

FIGURE 2: The resistivity of solutions of NaCl as a function of concentration and temperature (Flóvenz et al., 2012; based on Keller and Frischknecht, 1966)

Porosity is defined as the ratio of pores to the total volume of the rock. The degree of its interconnectedness (effective porosity) affects its effectiveness in enhancing conductivity in the rock matrix. Electric conduction in water-saturated porous rocks occurs mainly along pores of interconnected fractures in a volcanic zone. The resistivity of porous rock is correlated to porosity by the inverse square given by Archie's law (Archie, 1942):

$$\rho = \rho_w a t \varphi_t{}^{-n} \tag{3}$$

where ρ = Bulk (measured) resistivity (Ωm);
ρ_w = Resistivity of the pore fluid (Ωm);
φ_t = Fracture porosity as a proportion of the total volume;
a = Empirical parameter (°C^{-1});
t = Temperature (°C);
n = Cementing factor, an empirical parameter.

2.1 Salinity

Equivalent salinity of NaCl is used to illustrate the relationship between conductivity and salinity at different temperatures since NaCl is the dominant conductive species in geothermal fluids at depth (Ussher et al., 2000). The conduction is by mobile ions in a salt solution. Figure 2 shows the linear relationship between salinity and conductivity as expressed in Equation 4:

$$\sigma \approx \frac{C}{10} \tag{4}$$

where C (g l^{-1}) is the concentration of NaCl until at very high salinities beyond that of a geothermal reservoir.

2.2 Temperature

Resistivity of an aqueous solution at temperature 0-200°C decreases with increasing temperature, due to the increasing mobility of the ions caused by a decrease in the viscosity of the water (Figure 3).

For temperatures above 150°C, the mobility of free charges is affected by changes in viscosity, density and dielectric permittivity of the water causing conductivity to diverge from a linear relationship (Figure 2) and decreases with increasing temperature above 250°C (Flóvenz et al., 2012).

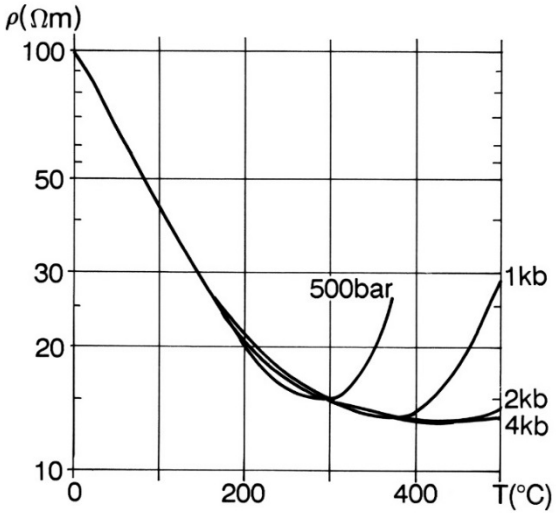

FIGURE 3: Resistivity of a NaCl solution as a function of temperature and pressure (Flóvenz et al., 2012; based on Quist and Marshall, 1968)

As depth increases, porosity and permeability decrease due to an increase in pressure. Pore fluid in the rock enters into a vapour phase because of the high temperature and pressure. Hence, at great depth in the crust and mantle, water is not a major medium of conduction. In most of the minerals, at depth, conductivity increases exponentially with an increase in temperature but decreases with pressure (Vozoff, 1990); this relationship was given in an Arrhenius formula and is illustrated in Figure 3:

$$\sigma = \sigma_O e^{-\left[\frac{(E_a + P\Delta V)}{kT}\right]} \tag{5}$$

where σ = Matrix conductivity (S/m);
σ_o = Conductivity at infinite temperature (S/m);
E_a = Activation energy (J);
P = Pressure (Pa);
ΔV = Activation volume (m^3);
k = Boltzmann's constant (m^2 $kg/s^{-2}K^{-1}$);
T = Absolute temperature (K).

When basalts are subjected to a temperature in the range of 400-900°C in a laboratory study, it gives E_a (0.8) and σ (300). This indicates that the rock resistivity is in the order of 1000 Ωm at 400°C and decreases to 10 Ωm at 800°C. Further increase in temperature will cause partial melts in the rock matrix and decrease the resistivity. In a geothermal environment where temperatures above 400°C are expected in the root of the system, the matrix conductivity will influence the overall conductivity (Flóvenz et al., 2012).

2.3 Resistivity of high-temperature areas and alterations

In a typical high-temperature geothermal system, resistivity is high in unaltered cold formations near the surface. As temperature progressively increases from 50 to 100°C with depth, low-temperature mineral alterations such as smectite and zeolites are formed making the rocks conductive due to their loosely bound cations. Resistivity increases again at moderately high temperatures of about 230-240°C, where the clay minerals are gradually replaced by chlorite as the dominant alteration minerals in the transition zone of mixed-clay layers. At higher temperatures exceeding 250°C, epidote and chlorite dominate, and the system is more resistive due to the bounded ions in the crystal lattice (Árnason et al., 2010).

The primary minerals in the host rock matrix are transformed into different minerals because of water–rock interaction and chemical transport by the geothermal fluids. Formation of alteration minerals depends on temperature, the types of primary minerals and the chemical composition of the geothermal fluid while the intensity of alteration is controlled by porosity and permeability (Flóvenz et al., 2012). The relationship between resistivity, tempera-ture, alteration and the conduction mechanism in a typical high-temperature basalt-dominated volcanic geothermal field is synopsized in Figure 4.

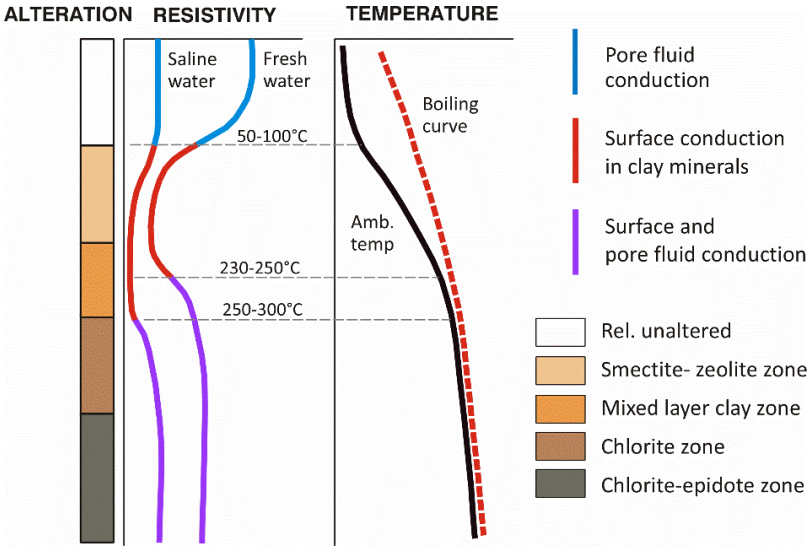

FIGURE 4: General subsurface resistivity, hydrothermal alteration, temperature, and conduction mechanism of the basaltic crust in Iceland (Flóvenz et al., 2012; based on Flóvenz et al., 2005)

For a long time researchers all over the world were puzzled by the high-resistivity core at depth which could not really be explained. It was expected that resistivity would decrease with an increase in temperature at depth until the late 80s when the cause of the resistive core at depth was established as being due to high-temperature alteration minerals; this became a model to be used all over the world in high-temperature volcanic systems (Figure 5). If the temperature that formed alteration minerals prevails, then subsurface temperature can be projected from resistivity structures. Thus, a resistivity structure is regarded as exhibiting the ultimate temperature since alteration is not affected by cooling in general. When alteration minerals indicate lower temperature than that measured in a well, it shows an immature system still undergoing heating up with alteration lagging behind, hence, not being in thermal equilibrium yet. However, when alteration minerals show higher temperature than that measured in a well, it is an indication of cooling in the system (Árnason et al., 2010 and Flóvenz et al., 2012). It is, therefore, prudent to not only confirm the shallow conductors and the resistive core but more importantly the deep-sited heat source before drilling to confirm the resources during geophysical surveys.

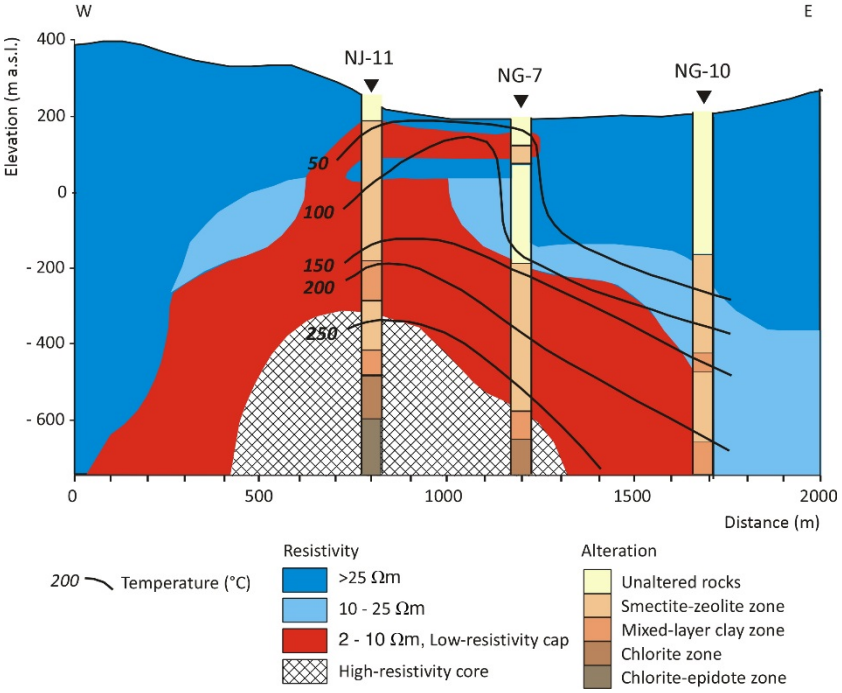

FIGURE 5: Classic example of a high-temperature geothermal system showing a resistivity cross-section from Nesjavellir geothermal field, SW-Iceland, alteration zoning and temperature (Árnason et al., 1987)

Hersir and Árnason (2009) indicated that similar resistivity structures in high-temperature geothermal fields hosted in volcanic rocks were globally characterized by convex structures. The general picture is of a low-resistivity zone doming up in the outer margin of a reservoir, underlain by higher resistivity and a resistive core. This is shown in Figure 5, which comes from a DC resistivity survey conducted in the Nesjavellir area, SW-Iceland in 1985 and 1986, detailing the picture of the resistivity structure in the uppermost 1 km compared with data from nearby boreholes.

3. RESISTIVITY SURVEY AND DATA COLLECTION

The use of resistivity methods in geothermal research started in the 1940s; by the 1960s these were the most important geophysical methods in surface exploration, delineating geothermal resources and production fields. The parameter of interest is the electrical resistivity which, in geothermal areas, gives information on temperature and rock alteration with depth, the major factors for understanding geothermal systems (Georgsson and Karlsdóttir, 2009).

The main principle common to all electrical methods is that electrical current is induced into the earth either directly (DC) or indirectly from a control source (TEM) or a natural source (MT) which generates an electromagnetic signal that is monitored at the surface (Georgsson and Karlsdóttir, 2009). In mapping resistivity variations with depth, sounding methods are used while profiling is applied to measure lateral variation of resistivity along a profile. The most important methods currently in use will be discussed in this chapter.

3.1 DC methods: Schlumberger sounding

Current is injected into the earth through electrodes at the surface (Figure 6a) generating an electrical field measured in square wave response (Figure 6b). Based on the geometry of the set-up, the electrical resistivity of the rock structures below is calculated from Ohm's law, (Equation 1). For a homogeneous earth and a single current source, the relevant equation for the electrical potential, V, at a distance, r, from the current source I, becomes:

$$V_r = \frac{\rho I}{2\pi r} \quad or \quad \rho = 2\pi r \cdot V_r / I \tag{6}$$

However, the earth is not homogeneous and what is measured is an average resistivity of the subsurface down to a certain depth penetrated by the current, called the apparent resistivity (ρ_a). Using Equation 6 above, the apparent resistivity can be derived:

$$\rho_a = \frac{\Delta V}{I} \cdot \frac{(S^2 - P^2)\pi}{2P} = K\Delta V / I \tag{7}$$

where S =AB/2 and P=MN/2 , ΔV is the potential difference and K is a geometrical factor.

The basis of operation in Schlumberger soundings lies in the configuration array shown in Figure 6a where the pairs of potential electrodes (MN) are maintained around the centre of the array. Moving MN is not recommended unless it is absolutely necessary to boost the measured signal while maintaining 20% of the distance between current electrodes (Georgsson and Karlsdóttir, 2009). The current electrodes (AB) diverge from the centre in equi-distance in both directions while the distance is increased in steps until the desired current length is reached. The depth of penetration increases with an increase in distance between A and B, which is about 1/3 of the distance between the current electrodes. The results from the response are plotted on a log-log scale for apparent resistivity as a function of AB/2 with increasing distance of separation for interpretation.

3.2 TEM method

The principle of operation in the TEM method is well explained in reports by Árnason (1989) and McNeill (1994). It involves transmitting a steady current sourced from a generator or battery pack into an insulated large square loop (300 m × 300 m) laid on the ground (Figure 7) that builds up a magnetic field of known strength. The current in the loop is abruptly turned off in a fraction of a second before it is turned on again. When the current is off, the built-up magnetic field in the loop starts to decay. The resultant decaying primary magnetic field induces secondary electrical currents (eddy currents) in the ground which further induce a secondary magnetic field decaying with time. The current distribution and decay rate of the secondary magnetic field depends on the subsurface resistivity structure of the earth (Árnason, 1989) and the response is monitored on the ground surface by measuring induced voltage in a receiver coil at the centre of the transmitter loop in time gates, as shown in Figure 8. The induced currents are shallow at early time (initial time when a strong eddy current is formed immediately after turn off, close to the transmitter loop) when the current is confined to the transmitter loop, while at late time (when the eddy current has decayed, weakened and travelled down with time) it radiates deeper and away from the loop. Current travels faster in resistive media and slows down within conductive layers (Rowland, 2002).

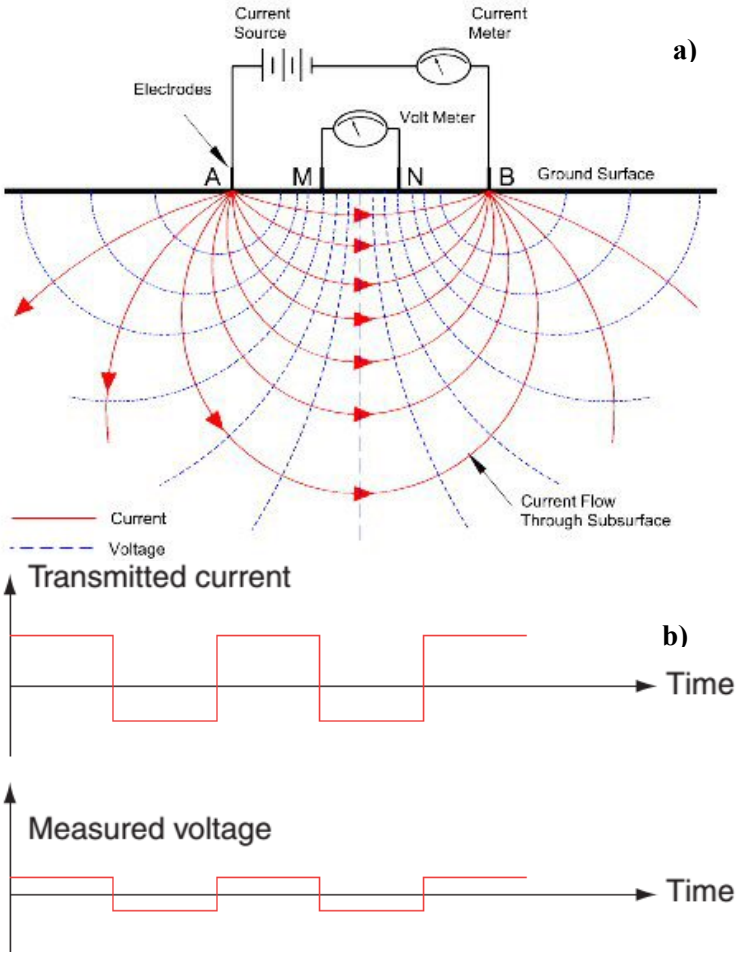

FIGURE 6: a) Field layout Schlumberger (NGA, 2013); b) typical half-duty square wave current and the corresponding potential signal (Flóvenz et al., 2012)

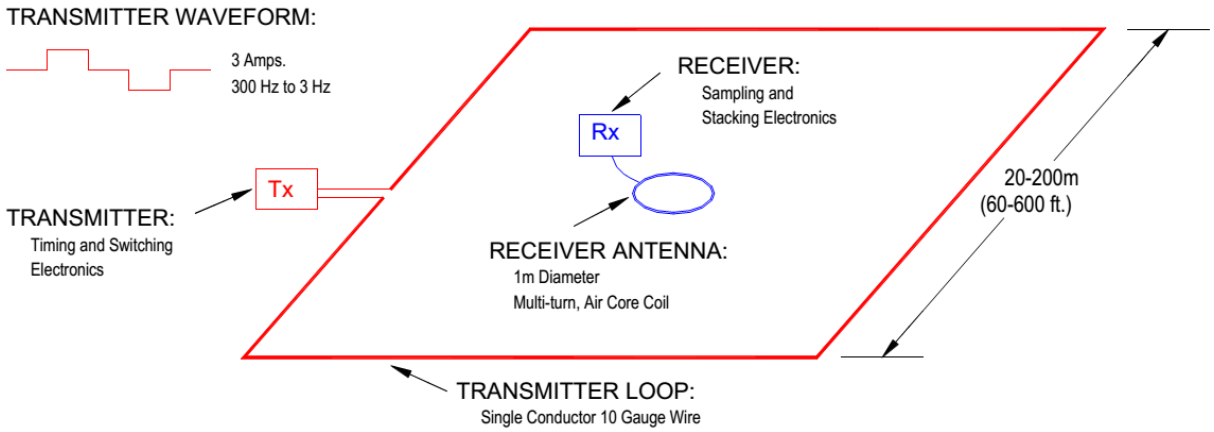

FIGURE 7: TEM field layout (Rowland, 2013)

The depth of penetration depends on the length of induction in the receiver coil after the current is turned off before it get noisy, and the resistivity of the subsurface stratum (Árnason, 2006a; McNeill, 1994). Thus, a low-resistivity stratum will require a longer period of time than the high-resistivity stratum to probe the same depth. Current is turned off linearly in a designated (TOFF) time interval measured by the transmitter and fed to the receiver manually to minimize infinite voltage induction in the source loop when turn off is sudden (Árnason, 1989).

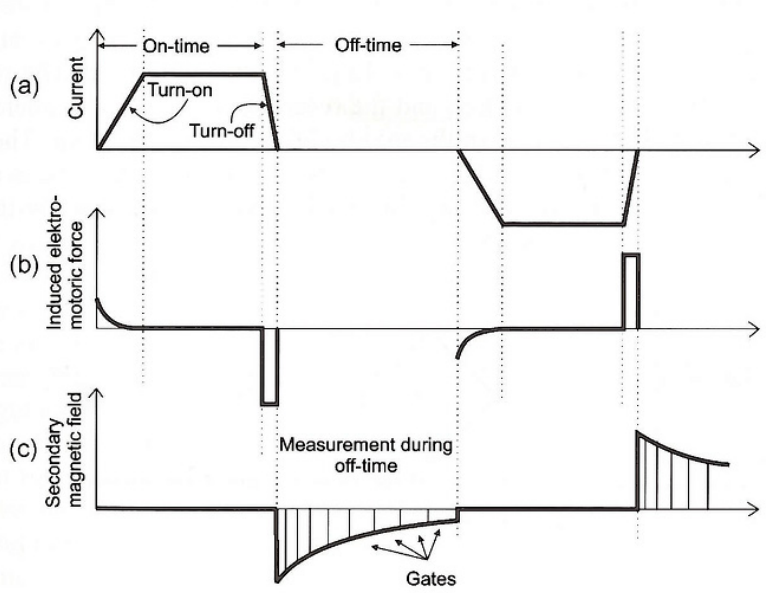

FIGURE 8: Basic principles of TEM method: a) Current flow in the transmitter loop; b) Induced e.m.f. in the ground; c) Secondary magnetic field measured after the current is turned off in the receiver coil assumed to be at the centre of the transmitter loop (Christensen et al., 2006)

3.2.1 Response curves for a homogeneous earth

The induced voltage in a receiver coil at late time in a homogeneous half space of conductivity, σ, is given by Árnason (1989):

$$V_{t,\,r} = I_o \frac{C(\mu_o \sigma r^2)^{3/2}}{10\pi^{\frac{1}{2}} t^{\frac{5}{2}}} \tag{7}$$

where

$$C = A_r n_r A_s n_s \frac{\mu_o}{2\pi r^3} \tag{8}$$

where t = Elapsed time after the transmitter current is turned off (s);
r = Radius of the transmitter loop (m);
A_r = Cross-sectional area of the receiver coil (m^2);
n_r = Number of windings in the receiver coil;
μ_o = Magnetic permeability in vacuum (H/m);
A_s = Cross-sectional area of the transmitter loop (m^2);
n_s = Number of windings in the transmitter loop;
I_o = Transmitted current (A);
$V_{t,r}$ = Measured voltage (V).

Equation 8 simulates characteristics of decaying induced voltage through time. The response measured in the receiver coil in a 1, 10 and 100 Ωm resistivity half space is shown in Figure 9 where the induced voltage is steady earlier in time but decreases with time until it reaches late time when induced voltage (V_t) decreases linearly as a function of time (t) logarithmically with a gradient of -5/2. Thus, induced voltage $V(t)$ in a receiver for a late time homogeneous half space with conductivity (σ) is proportional to $t^{-5/2}$ and $\sigma^{3/2}$ as seen in Equation 8. The response in early times depends on resistivity because it increases with an increase in resistivity (Árnason, 1989).

Figure 10 shows apparent resistivity approaching true resistivity of a homogeneous half space at late time as resistivity values reduce and the receiver voltage increases due to the presence of all the current after turn off. Apparent resistivity is based on the time behaviour of the receiver coil output voltage at

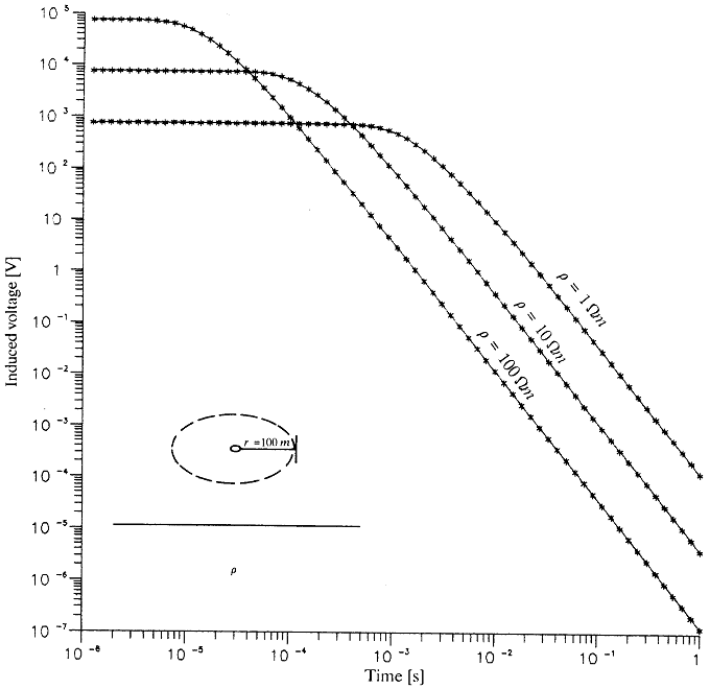

FIGURE 9: Voltage response for a homogeneous half-space (Árnason, 1989)

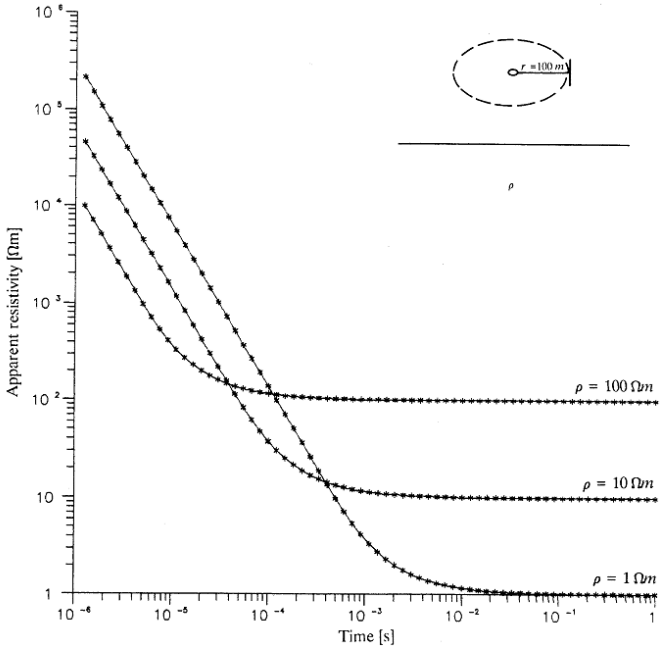

FIGURE 10: Late time apparent resistivity for a homogeneous half-space (Árnason, 1989)

late time when it decays as $t^{-5/2}$. At early time when current is entirely in the upper layers, the receiver voltage is too low, thus apparent resistivity is too high (McNeill, 1994). Apparent resistivity, ρ_a, of a homogeneous half-space in terms of induced voltage at late times after the source current is turned off is given by (Árnason, 1989):

$$\rho_a = \frac{\mu_o}{4\pi}\left[\frac{2\mu_o A_r n_r A_s n_s I_o}{5t^{5/2}V_{t,r}}\right]^{\frac{2}{3}} \qquad (9)$$

3.2.2 TEM data acquisition

The TEM data from Suswa field were collected using equipment from Zonge and Phoenix Geophysics (V8). The setup is shown in Figure 7. A loop of 300 m × 300 m was laid out on the ground by at least two field crew members in a square configuration from a common point where the current source is located. Transmitter and receiver are synchronized using crystal clocks (in-built) so that the receiver knows the exact current turn off time (generated when synchronizing and manually fed into the receiver by the surveyor) to begin recording the decaying voltage. The transmitter and receiver were set to the same frequency while the loop was being laid out to ensure cross communication between them in transmitting and receiving signals. Once the loop was connected, the generator was turned on to transmitted current (10 A) to build-up a strong magnetic field in the loop. The receiver loop and coil were transferred to the centre of the loop, located 212 m from the transmitter for 300 m by 300 m, and 140 m for 200 m by 200 m loop. At the centre of the loop where the readings were recorded through the receiver coil, data were acquired in low and high frequencies. At low frequency, the TEM probes much deeper and is less influenced by near surface cultural noise, while at high frequencies it measures at shallow depths. Before changing to high frequency reading, the transmitter frequency is manually adjusted before proceeding with data collection in the next frequency phase to ensure the signals transmitted are received at the same frequencies or else no data are collected.

Different coil sizes were used to maximize the receiver readings at different frequencies. A small coil was used to probe at shallow depths at high frequency without saturating the voltage since the current

induced was less. At low frequency reading, the bigger loop induces more current and measures the response at depth in the late time before the signal weakens and is drowned into noise. In shallow depths, a small loop is more effective than a bigger loop, while at great depth the bigger loop is more advantageous. The data were automatically saved in the receiver to be downloaded and processed for inversion and interpretation.

3.3 MT Method

Magnetotelluric (MT) was pioneered by Tikhonov (1950) and Cagniard (1953) in Russia and France, respectively. It is an electromagnetic method that probes electro-stratigraphic structures of the earth from shallow depths to hundreds of kilometres (Hersir and Árnason, 2010). Thus, the basic application of the MT method is to determine the subsurface electrical conductivity of the complex earth from measurements of natural transient magnetic (**H**) and electric (**E**) fields on the surface in orthogonal direction (Hersir and Árnason, 2010).

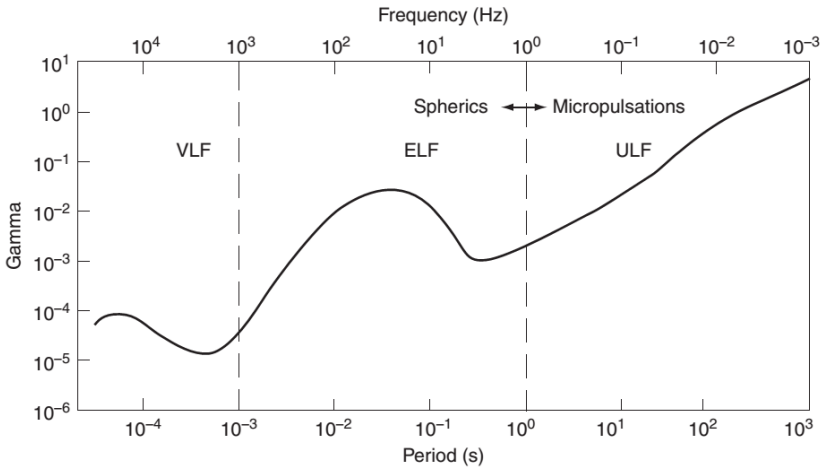

FIGURE 11: Electromagnetic frequency ranges (Flóvenz et al., 2012)

MT superiority over the rest of electrical methods is due to its great depth of subsurface penetration which depends on the range of period it operates in. The longer the period of measurement, the higher is the depth of penetration. Thus, three main categories of 5 channel Magnetotelluric units are classified according to ranges of frequencies/periods they operate in which also determine the depth of penetration (Figure 11). MT operates in the range of 400 Hz – 0.0001 Hz, Audio-MT 100 Hz – 10 kHz and LMT - long period (1000 – 10,000 s). The MT method is passive and uses natural magnetic variations in the geomagnetic field of the earth as its signal source and has no external source of power in its operation except for the data logger powered by batteries.

3.3.1 Sources of the earth's electromagnetic fields

The spectrum of the earth's electromagnetic field varies widely between high and low frequencies. The source of low frequencies (long periods) is ionospheric and magnetospheric currents due to solar wind interference with the earth´s magnetic field while high frequencies (short periods) greater than 1Hz are caused by thunderstorms near the equator and distributed as guided waves between the earth and the ionosphere (Hersir and Árnason, 2010).

3.3.2 Field setup and data acquisition

The know-how on instrumentation (Figure 12), data acquisition, processing and interpretation is the fundamental step in the effective use of magnetotelluric equipment which will be highlighted in this report. The main components of a 5-channel

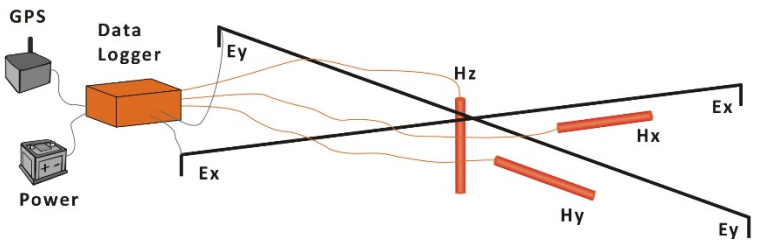

FIGURE 12: Magnetotelluric setup for data acquisition (Flóvenz et al., 2012)

MT data acquisition unit instrument (MTU-5) from Phoenix Geophysics are a data logger (MTU), 2 pairs of electric lines (E_x and E_y) which measure the electric potential differences between the electrode pairs, and 3 magnetic coils (H_x, H_y and H_z) which are sensors for measuring magnetic variations. One pair of electric lines (E_x) is oriented in the N-S magnetic direction while the (E_y) lines are oriented along the E-W magnetic direction. Porous pot electrodes with porous ceramic bottoms at the end of each electric line with $PbCl_2$ solutions installed in wet pits with a solution of NaCl to reduce ground resistance and noise is well illustrated in Phoenix Geophysics' users guide manual (2005). A Global Positioning System (GPS) satellite synchronizes the data, which are recorded and saved onto a data logger in time series digital format into a memory flash card (Flóvenz et al., 2012). A fully charged 12 V battery powers the data logger over the period of data collection, mostly overnight.

In addition to the setup shown in Figure 12, a waterproof canvas is required to cover the battery and data logger to protect the duo from direct contact with water and dust. A compass for orienting the magnetic and electric sensors in horizontal and orthogonal directions and markers (stick) to enhance alignment when orienting electric and magnetic lines are vital. To ensure the magnetic sensors are horizontally laid (H_x and H_y) and that H_z is vertical, a spirit level is used.

MT equipment is calibrated before the start of a new field survey to ensure the equipment is in good working condition and is normalized to the environment for the survey. Both the box (MTU) and magnetic coil sensors are calibrated.

3.3.3 Basic principles

In principle, a naturally occurring time varying fluctuating magnetic field induces an electrical field which further induces an eddy current in the ground, measured on the surface in horizontal (E_x) and orthogonal (E_y) directions. The electric fields are induced by the corresponding source magnetic fields (E_xH_y and E_yH_x) orthogonally (Flóvenz et al., 2012); thus, by measuring variations in the magnetic and electrical fields on the surface, subsurface resistivity and phase as a function of the frequency of the electromagnetic field are determined using the four basic Maxwell equations given below:

Faraday's law:

$$\nabla \boldsymbol{E} = \mu \frac{\partial \boldsymbol{H}}{\partial t} \tag{10}$$

Ampere´s law:

$$\nabla \boldsymbol{H} = j + \varepsilon \frac{\partial \boldsymbol{E}}{\partial t} \tag{11}$$

Gauss´s law (electric field):

$$\text{div}\, \boldsymbol{D} = \eta \tag{12}$$

Gauss´s law (magnetic field):

$$\text{div}\, \boldsymbol{B} = 0 \tag{13}$$

where $\boldsymbol{E}$ = Electrical field (V/m);
$\boldsymbol{B}$ = Magnetic intensity (A/m);
$\boldsymbol{j}$ = Electrical current intensity (A/m^2), and
$\boldsymbol{j}$ = $\sigma \boldsymbol{E}$;
μ = Magnetic permeability (H/m);
ε = Electric permittivity (F/m);
$\boldsymbol{D}$ = $\varepsilon \boldsymbol{E}$; and
$\boldsymbol{B}$ = $\mu \boldsymbol{H}$.

3.3.4 Impedance tensor and dimensionality

The impedance tensor (Z) relates the orthogonal components of the horizontal electric and magnetic fields using Maxwell equations to generate resistivity of a homogeneous half space. The phase difference between E_x and H_y is equal to $\frac{\pi}{4} = 45°$.

$$\begin{pmatrix} E_x \\ E_y \end{pmatrix} = \begin{pmatrix} Z_{xx} & Z_{xy} \\ Z_{yx} & Z_{yy} \end{pmatrix} \begin{pmatrix} H_x \\ H_y \end{pmatrix} (\boldsymbol{E = ZH}) \tag{14}$$

$$E_x = Z_{xx}H_x + Z_{xy}H_y \tag{15}$$

$$E_y = Z_{yx}H_x + Z_{yy}H_y \tag{16}$$

$$Z_{xy} = \frac{E_x}{H_y} = \sqrt{\omega\mu\rho}\ e^{i\pi/4}\ and\ Z_{yx} = \frac{E_y}{H_x} = -Z_{xy} \tag{17}$$

where Z = Impedance tensor;
$\pi/4$ = Phase difference between the electric and the magnetic field;
$Z_{xy}\ and\ Z_{yx}$ = Characteristic impedance in x and y directions;
ω = Angular frequency ($2\pi f$) where f is frequency (Hz);
μ = Magnetic permeability (H/m);
E_{xy} = Electric field intensity (V/m) in x, y direction;
H_{xy} = Magnetic field intensity (A/m) in x, y direction.

Each component of the impedance tensor, Z_{ij}, is composed of real and imaginary parts. They have both magnitude and phase.

Resistivity of a homogeneous half space is given by:

$$\rho_{xy} = \frac{1}{\omega\mu}\left|Z_{xy}\right|^2 = \rho_{yx} = \frac{1}{\omega\mu}\left|Z_{yx}\right|^2 = \rho \tag{18}$$

For an inhomogeneous earth, the apparent resistivity (ρ_a) and phase (θ_a) as a function of frequency can be defined as if the earth was homogeneous using this same formula. In an inhomogeneous earth, the resistivity, ρ, in the Equation above can be written as:

$$\rho_a = 0.2T|Z|^2;\ \theta = \arg(Z) \neq 45° \tag{19}$$

The apparent resistivity calculated from the off-diagonal elements of the impedance tensor in Equations 18 and 19 are the same for a homogeneous 1D earth. Rotating the impedance tensor for a non-1D earth will change the resistivity values of ρ_{xy} and ρ_{yx}. Thus, during the inversion process, they will give two different models, neither of them necessarily being the correct one. Hence, the rotationally invariant determinant of the impedance tensor, which is a kind of an average value of the apparent resistivity and phase, is used here in the inversion to produce the model (Badilla, 2011). The determinant of the apparent resistivity and phase is calculated by:

$$\rho_{det} = \frac{1}{\omega\mu}|Z_{det}|^2 = \frac{1}{\omega\mu}\left|\sqrt{Z_{xx}Z_{yy} - Z_{xy}Z_{yx}}\right|^2\ ;\ \theta_{det} = \arg(Z_{det}) \tag{20}$$

3.3.5 Skin depth

The depth below the surface of the conductor where the electromagnetic field has decreased to e^{-1} of its original value is called the skin depth. It is expressed as:

$$\delta=500\sqrt{\rho T} \quad \text{(m)} \tag{21}$$

where δ is the skin depth (m), ρ is the resistivity of the medium (Ωm) and T is the period (s).

The expression indicates estimated depth of penetration and depends on resistivity and period; the larger the period the deeper the sounding detects the subsurface resistivity.

3.3.6 2D earth

In a 2D earth environment, resistivity varies with depth and in one lateral direction. It is constant in the other horizontal direction (along the electrical strike). MT impedance tensor data are mathematically rotated with one axis perpendicular to the electrical strike and the other axis is parallel to it, by minimizing the off diagonal elements of the impedance tensor. So $Z_{xx} = Z_{yy}=0$, like in the 1D case, but the difference is that, in 2D, $Z_{xy} \neq -Z_{yx}$:

$$Z_{2D} = \begin{pmatrix} Z_{xx} & Z_{xy} \\ Z_{yx} & Z_{yy} \end{pmatrix} \text{ rotated to give } Z_{2D} = \begin{pmatrix} 0 & Z_{xy} \\ Z_{yx} & 0 \end{pmatrix} \tag{22}$$

In 2D the field is split into two independent impedance tensor modes: E- and B-polarization. Transverse Electric (TE) mode or E-polarization is when the electric field is parallel to the electromagnetic strike and Transverse Magnetic (TM) mode or B-polarization is when the magnetic field is parallel to the electromagnetic strike.

In a 3D case, resistivity varies in all three directions, that is $Z_{xx} \neq Z_{yy}$ and $Z_{xy} \neq -Z_{yx}$ with no possible rotational direction that minimizes the diagonal components to zero (0) at the same time.

Swift skew is expressed below and gives an indication of 1D, 2D or 3D subsurface environment depending on the calculated value of S. Large S value indicates 3D and a small value indicates 1D and 2D:

$$\text{Skew} = \text{S} = \frac{|Z_{xx} + Z_{yy}|}{|Z_{xy} - Z_{yx}|} \tag{23}$$

3.3.7 Strike analysis

The electrical strike direction shown in Figure 13 is an indication of where the resistivity changes least often in the same direction as the geological strike direction of the survey area. The figure shows alignment along the low-resistivity anomaly within the caldera rim, indicating ring structures (e.g. see Figure 29). The Z-strike is achieved by minimizing the diagonal impedance tensor elements (Z_{xx} and Z_{yy} or maximizing the off diagonal elements Z_{xy} and Z_{yx}). However, there is 90° ambiguity in geoelectric strike (i.e. Z-strike) which is fixed

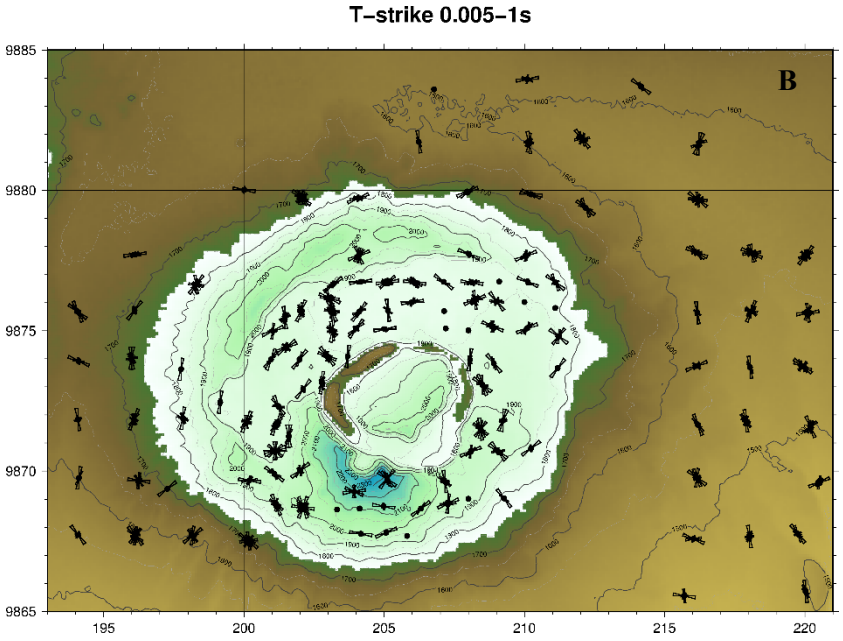

FIGURE 13: Rose diagram for electrical strike direction based on Tipper strike at 0.005-1 s

by measuring H_z and calculating the Tipper strike as shown in Equation 24 (Hersir et al., 2013) and Figure 14:

$$H_z = T_x H_x + T_y H_y \tag{24}$$

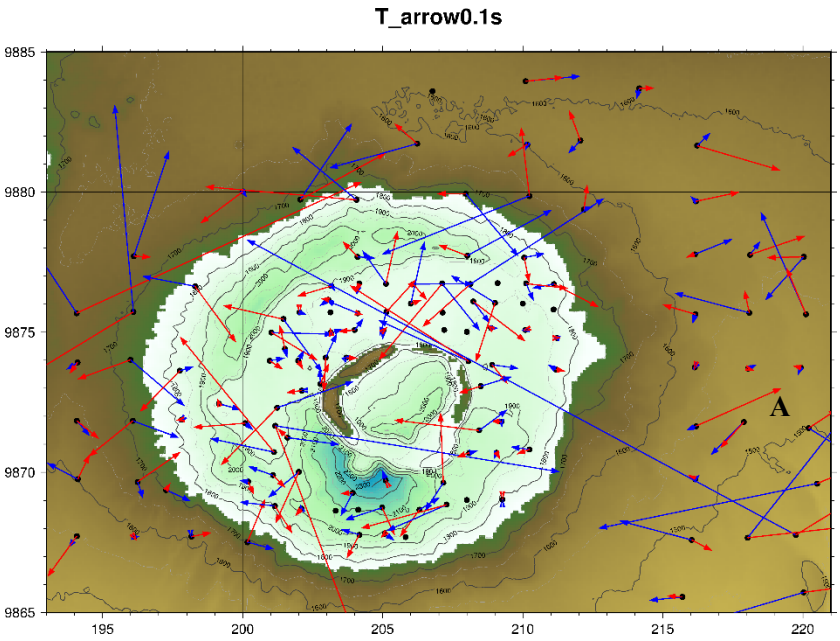

FIGURE 14: Induction arrows at shallow depth (0.1 s) pointing away from the caldera rim

Figure 14 is an example of induction arrows; the blue arrows are the real and the red are the imaginary part. The blue arrows point away from the conductor at shallow depth within the ring structure.

3.3.8 Static shift

The static shift problem is common in resistivity methods that measure voltage (electric field) over a short distance on the earth's surface and are due to in-homogeneities in resistivity close to the electrodes, like DC soundings and MT. The apparent resistivity is distorted by a multiplicative constant, *S*, which displays a shift when data are presented on a log scale as shown in Figure 15. In Suswa field, most MT data were shifted down (on average 0.8), shown on the histogram in Figure 16, due to near surface conductive bodies. Above the conductive bodies, the static shift multiplier (*S*) was less than 1, and the apparent resistivity curve shifted downward resulting in decreased depth to the boundaries. *S* higher than 1 results in higher resistivity and increased depth to the boundaries, causing an upward shift of apparent resistivity over resistive bodies (Árnason, 2008).

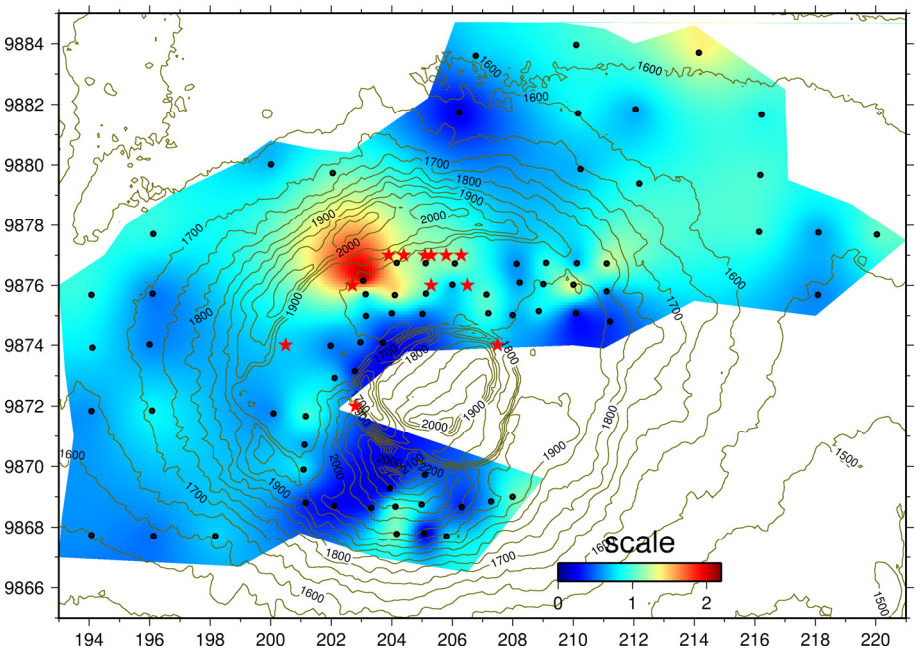

FIGURE 15: Static shift distribution map, black circles are MT/TEM locations and red stars are fumaroles

Two main causes of static shift are electric field and current distortion due to the near-surface contrast in topography that causes channelling effects that are common in a geothermal environment. In the upflow zone where conductive clay minerals form convex structures surrounded by resistive lava,

distortion may be common. The solution is to correct static shift in MT and DC data using transient electromagnetic data which are not affected by this problem (Árnason et al., 2010).

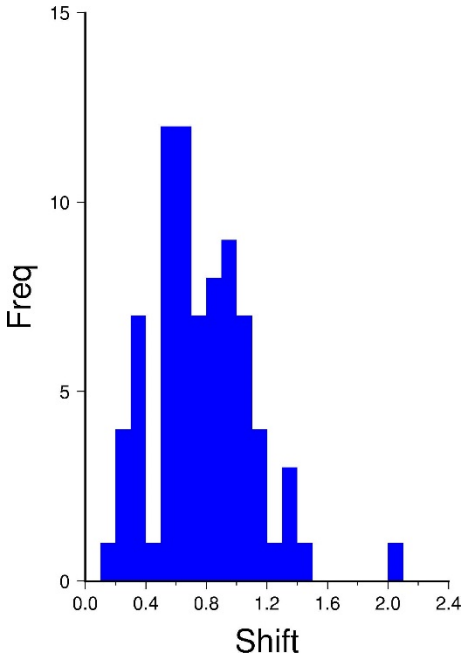

FIGURE 16 : Static shift histogram

4. PROCESSING AND INVERSION OF MT AND TEM DATA

4.1 MT data processing

The collected time series data downloaded from the MT equipment are quality scrutinized using the time series viewer option in the *SSMT2000* software (Phoenix Geophysics, 2005). This will give a first indication of the data quality that influences decision making on whether to repeat the sounding or not. Then parameter files (tbl) are edited to reflect the setup for the collected data. The resulting time series are Fourier transformed to the frequency domain, and then the different auto- and cross-powers are calculated using the robust processing method (RPM). The data are graphically edited using *MTEditor* Phoenix geophysics software by masking the outliers to achieve apparent resistivity and phase curves and other relevant parameters. The resulting MT parameters are all saved as EDI files ready for export to the interpretation software (see SEG, 1991). Figure 17 illustrates processed MT apparent resistivity and phase curves from the Suswa prospect. At periods below 0.1 s, it exhibited a 1D response where apparent resistivity values and phase decreased with increasing period. For periods above 0.1 s, the curves separated indicating a non-1D environment with one apparent resistivity increasing as the other decreased.

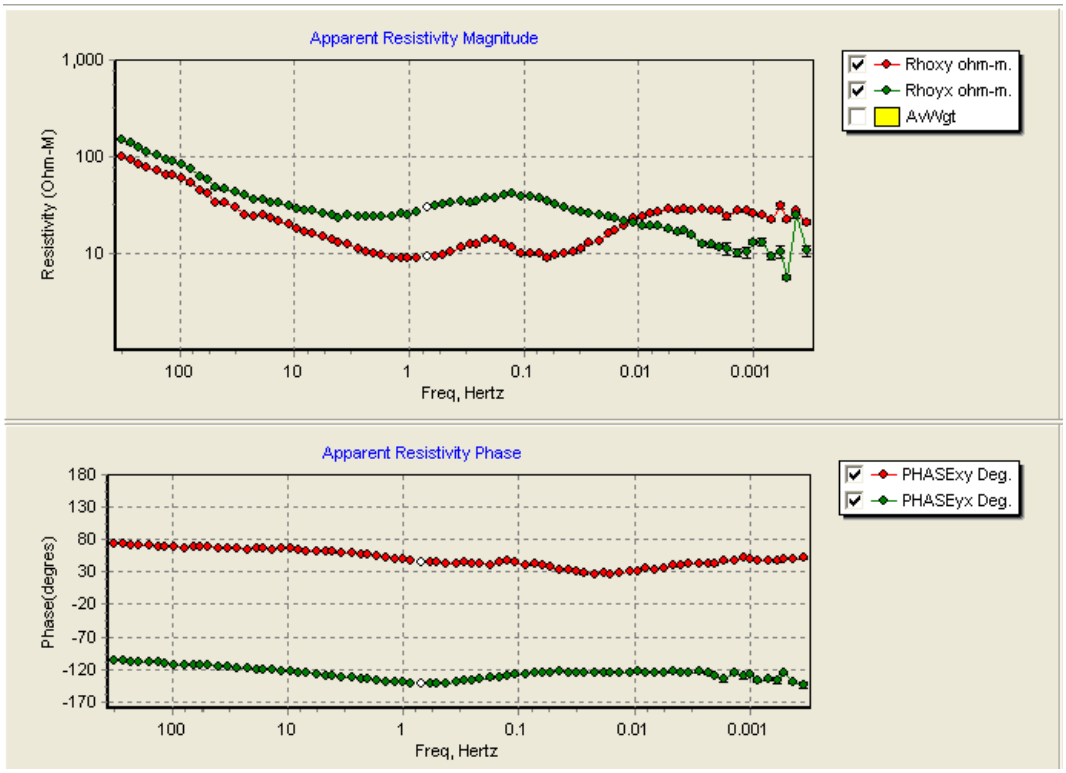

FIGURE 17: MTEditor output showing apparent resistivity and phase curves of Suswa sounding SUSMT94

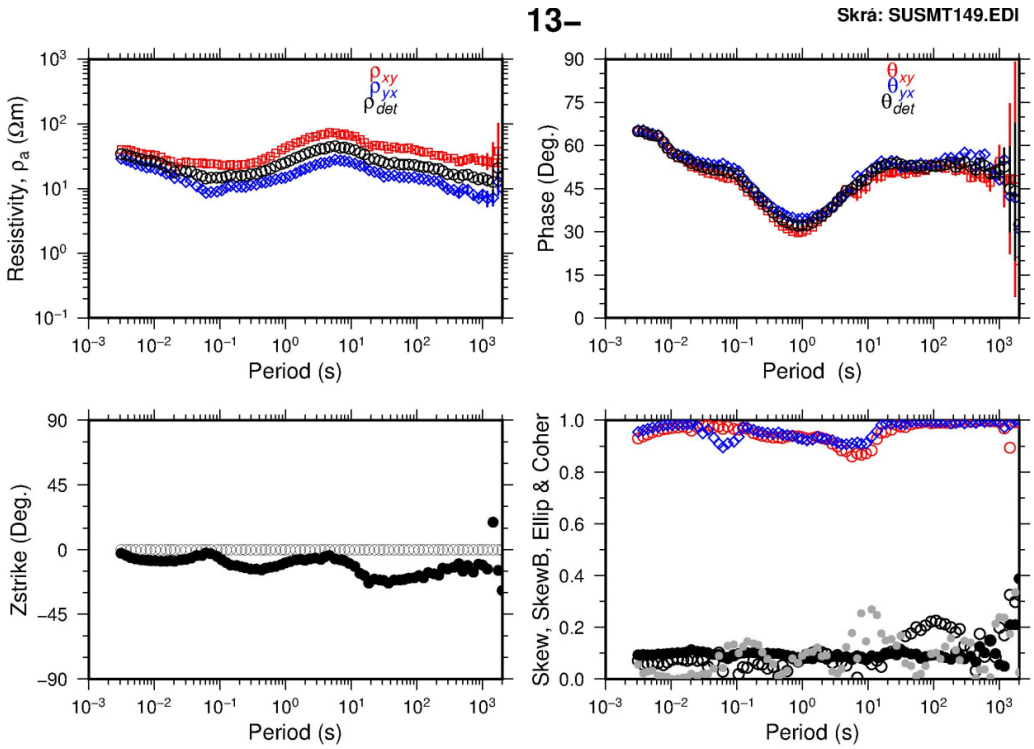

FIGURE 18: Processed MT data for sounding 149 (SUSMT149) from Suswa geothermal prospect, Kenya; The plots show the apparent resistivity and phase derived from the xy (red) and yx (blue) components of the impedance tensor and the determinant invariant (black), the Z-strike or Swift angle (black dots), and multiple coherency of xy (red) and yx (blue), and skew (black dots) and ellipticity (grey dots)

The Electronic Data Interchange (EDI) files produced by *MTEditor* are run through scripts developed at ISOR: *dos2unix*, changes the edi files from a window based environment to a Linux readable format and *spect2edi* calculates various parameters and produces the result in the standard EDI format which is ready for inversion in the *TEMTD* programme. Suswa data were also run through *edidatum* script to change the coordinates taken by GPS from WGS84 datum to Arc1960 for Kenya and *edi2ps* to generate PostScript graphs. Finally ps2raster transforms postscript files to PNG or JPEG figures. Figure 18 shows MT sounding SUSMT149 which has been run through the aforementioned Linux scripts, ready for *TEMTD* inversion software and is explained below. The remaining soundings are given in Appendix II (Mohamud, 2013).

4.3 1D inversion of TEM data

Figure 19 shows a typical inversion process. In the beginning only measured data and a guessed initial model are available. The initial model is run to test if the response fits the measured data. If the fit is good it becomes the final model and if not, the model is subjected to an iterative algorithm, where the parameters resistivity and thicknesses are adjusted. The inverted model is run again in a forward algorithm and compared several times in an iteration process which improves the model in a successive iteration until a good fit is obtained. In Árnason (1989), the details of the inversion algorithm are discussed. The TEMTD program uses damping parameters to smooth sharp steps and oscillations in the model values. Minimum structure Occam inversion is perfomed, where the number of layers and thicknesses are kept constant while the resistivity variation is

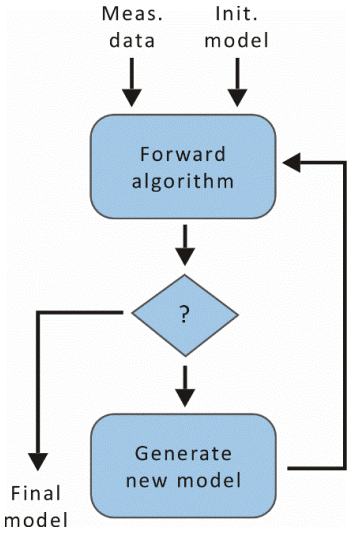

FIGURE 19: Sequence of the inversion process (Flóvenz et al., 2012)

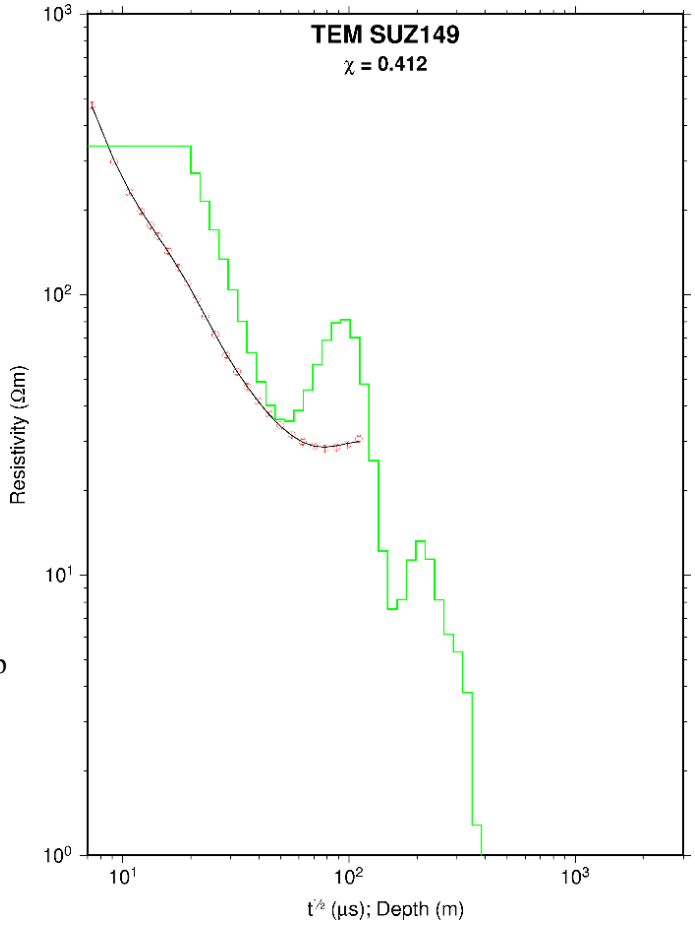

FIGURE 20: A TEM sounding (SUZ149) and its 1D Occam inversion from Suswa geothermal prospect area; red circles: measured late-time apparent resistivities (different datasets for different receiver loop sizes and current frequencies); black line: apparent resistivity calculated from the model shown in green; at the top of the figure is the misfit function; the root-mean-square difference between the measured and calculated values, $\chi = 0.412$

smoothed with damping parameters. Árnason (2006b) gives a detailed step by step procedure on 1D inversion of MT and TEM using *TEMTD* software developed at ISOR.

In this report, 72 TEM soundings from Suswa geothermal prospect were 1D inverted. An example is given in Figure 20. All of them can be found in Appendix I (Mohamud, 2013).

4.4 Joint inversion of MT and TEM data

To correct the static shift problem in MT data already discussed in the previous chapter, the MT inversion is run jointly with TEM data which is not affected by the static shift as it uses magnetic rather than electrical fields during data acquisition. The shift parameter is one of the parameters that is inverted for in TEMTD. Either an MT or TEM initial model is run from inverted or processed measured data to get started; then, from the model, an inversion algorithm is run as explained in Figure 19. Several parameters are adjusted until a good fit between MT and TEM curves are obtained. An example is given in Figure 21. The remaining jointly inverted soundings can be found in Appendix III (Mohamud, 2013).

In a perfectly static-shift free situation, the shift which is the ratio of MT to TEM distance of separation is 1. However, the earth is heterogeneous and in a low-resistivity near-surface environment the curves are shifted downwards with an S factor less than 1, and in a high-resistivity environment the curves shift upwards with an S value exceeding 1. The distance recommended between MT and TEM soundings to be used in joint inversion should not exceed 50-100 m.

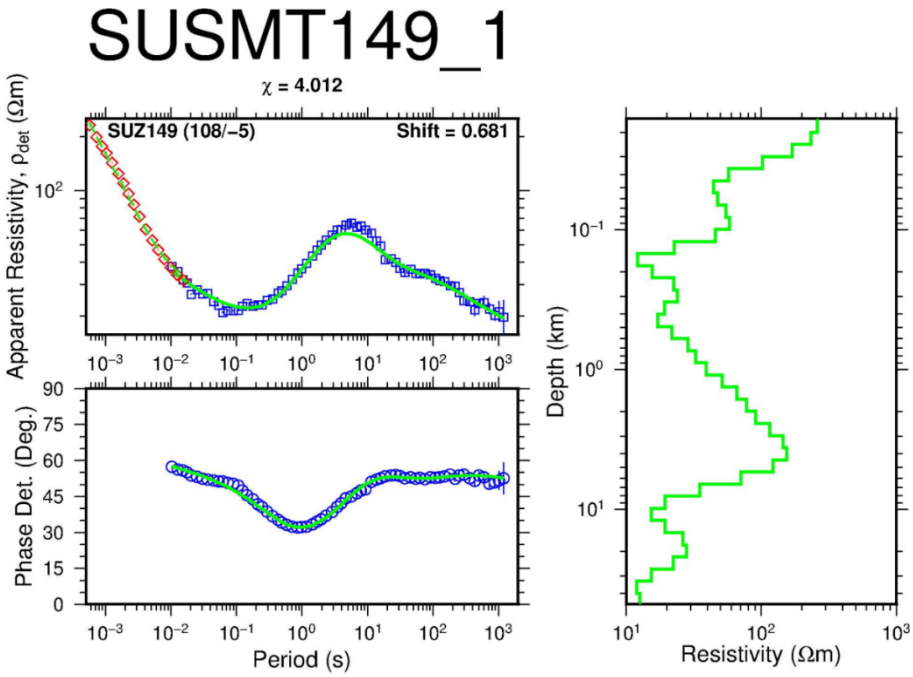

FIGURE 21: Joint 1D inversion of TEM and MT data: SUSMT149_1 is the MT station corresponding to TEM station SUZ149; red diamonds: measured TEM apparent resistivity; blue squares: measured MT determinant apparent resistivity; blue circles: apparent phase derived from the determinant of MT impedance tensor; green lines: on the right show the 1D resistivity inversion model, and to the left are its synthetic MT apparent resistivity and phase response; numbers in parentheses (108/-5) indicate the two stations were 108 m apart and their elevation difference was 5 m (- sign means TEM station is at higher elevation than MT); Chi square χ (4.012) is the misfit between the measured and calculated values in the models while 0.681 is the shift value

5. SUSWA GEOTHERMAL AREA

5.1 Geological and structural setting

The Kenya Rift is a volcano tectonic axis of continental scale that stretches from the Afar junction in the north to southern Africa. The Rift started 30 million years ago (Omenda, 1997). During the last 2 million years, intense volcanic activities in the Rift axis formed large shield volcanoes associated with high-temperature geothermal prospects in the Kenya Rift. The young volcanic formations in the Rift graben host shallow magmatic bodies beneath them which enhance the occurrence of geothermal activities in the rift zone (Omenda, 2007). Mt. Suswa is the southernmost volcano of the Kenya Dome (Figure 1), located 30 km south of Greater Olkaria Domes. The main surface geology in Suswa is trachyte, phonolite, ignimbrite, and volcanic ash.

The chronological occurrence of volcanic episodes in Mt. Suswa area was summarized by White et al. (2012) and discussed by several others (Espejel-García, 2009; and Omenda, 1997) in three major phases. The first phase was the initial eruption of predominantly trachyte lava flows derived from a central source with some phonolite that led to the formation of a shield volcano. The second phase was during cauldron subsidence (syn-caldera) that produced abundant pumice and thick lava flows from a ring fracture zone outside the caldera. The third eruptive phase is post caldera lavas that filled the caldera and resulted in Ol Doinyo Nyukie volcano. A collapse in the form of a concentric graben formed inside the older caldera towards the end of the last eruptive episode, seen in Figure 22.

The main structures in the area are N-S trending faults aligned with the main rift graben (Figure 23). The calderas form the main visible ring structures that seem to control the fumarolic activities on the walls of the outer caldera in the Kisharo area. Tandamara fault dissects the calderas into two halves oriented in a N-S direction, inferred from trachytic lava domes aligned on the northern slopes of Mt. Suswa (Omenda, 1997).

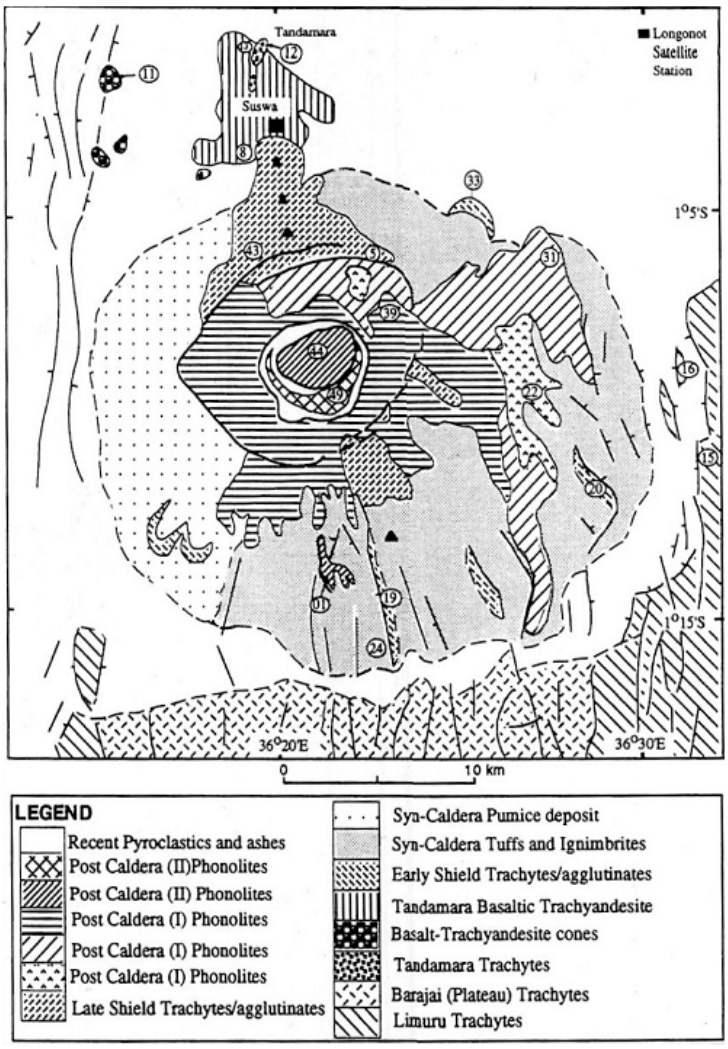

FIGURE 22: Suswa geology (Omenda, 1998)

5.2 Geothermal manifestations

Surface geothermal manifestations in Suswa are in the form of altered and hot grounds, the presence of geothermal grass, cinder cones, young lavas and fumaroles (GDC, 2013). The manifestations are located along the rim of the inner and outer caldera walls and on the floor and slopes of the outer caldera (see Figure 23). The fumarolic activities are stronger on the rim of outer caldera wall suggesting the presence of a structurally controlled hydrothermal system. However, manifestations outside the ring structures are weak fumaroles with low alteration and temperatures readings. The Mt. Suswa local community harvests water from condensed fumaroles as their source of water for domestic use.

5.3 Previous work

An interferometry synthetic aperture radar (InSAR) study by Biggs et al. (2009) between 1997 and 2008, to detect surface displacement of high resolution, showed subsidence of about 5 cm at Mt. Suswa between 1997 and 2000, indicative of an existing active magmatic system beneath it. Changing pressures within the crustal magma reservoirs caused by magma and/or volatile fluxes produce changes in volcano shape on the scale of centimetres to metres.

Gravity data analysis and interpretation by Cantini et al. (1990) indicated a NE-SW trending positive anomaly beneath the southern edge of the caldera with an amplitude of 30 mGal. The anomaly is presumably related to the heat source, postulated to be of basaltic melt magma directly beneath the caldera. The study also related identified linear positive anomalies showing structurally controlled shallow bodies in the basement of the Suswa volcanic activity.

Passive seismic data collected and analysed by Simiyu (1999) over a seismic network in the Suswa geothermal prospect area showed low seismic velocity values, interpreted to mean high heat flow,

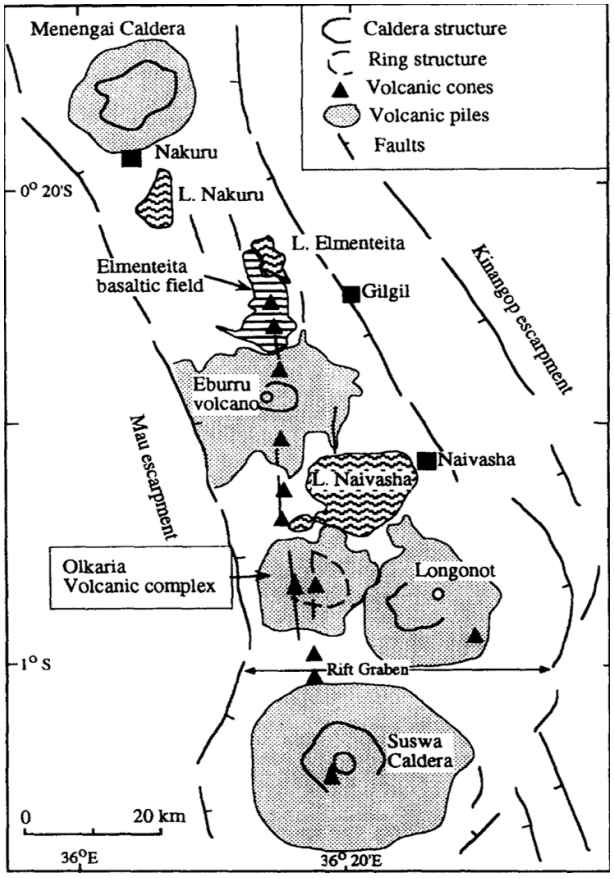

FIGURE 23: Structures of Suswa (Omenda, 1998)

fracturing of rocks and steam saturation. Simiyu (1999) further indicated seismicity gaps within the field mark zones, inferred to be hot magmatic intrusions that have raised the temperature above the brittle-ductile transition temperature of above 450°C.

Simiyu and Keller (1997) also indicated from research carried out by the Kenya Rift International Seismic Project (KRISP) in 1985 and 1990 that seismic events are at shallower depth and smaller on the axis but larger and deeper on the rift flanks south of Lake Naivasha, an area that encompasses Suswa. Figure 24 shows a high V_p velocity zone below the Suswa prospect.

Results from an integrated resistivity survey (MT and DC), Onacha et al. (2009) identified three anomalous areas: the southwest part of the caldera, the eastern slope and the northwest corner of the caldera close to the anticipated heat source. High-resistivity values noted from Suswa caldera rocks in comparison to Olkaria and Longonot areas were ascribed to lower alteration, lower bulk permeability and varied lithology. They further anticipated high vertical permeability due to recent caldera reactivation.

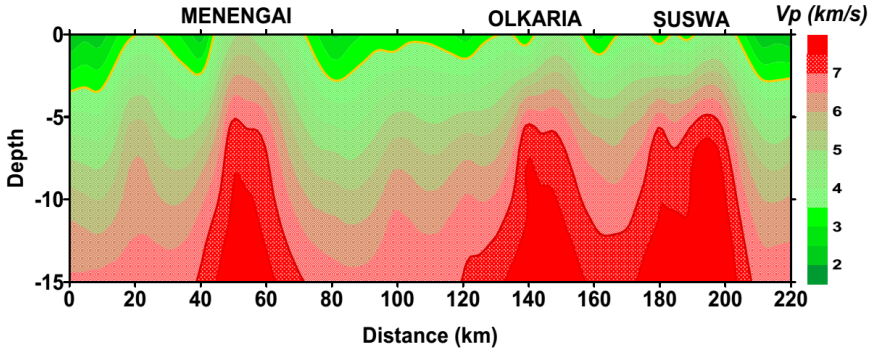

FIGURE 24: Seismic velocity model along the Rift axis showing high-velocity zones beneath Menengai, Olkaria and Suswa volcanic centres based on the KRISP 1985-1990 axial model by Simiyu, 2010, based on Simiyu and Keller, 2000

Scientific research, mainly in geology, have been carried out by different entities from PhD and Masters dissertations to geoscientific researches by Kenya Electricity Generating Company (KenGen) and more recently Geothermal Development Company (2013) in the search for geothermal resources. The current data used for this project are a part of 150 MT and 103 TEM soundings collected in a survey conducted in 2013. In this report, 72 data points of both MT and TEM soundings in the same location or within 200 m of each other were used. TEM was used for static shift correction of the MT data in 1D joint inversion of TEM and MT as described in the next chapter.

5.4 Suswa MT and TEM survey area

The survey points for both MT and TEM data, fumaroles and profiles for the cross-sections are shown in Figure 25. MT data were collected using Phoenix Geophysics equipment (MTU-5A) for a period of

about 22 hours. The survey was conducted between December 2012 and February 2013, covering 150 MT and 103 TEM soundings. In this survey two types of TEM equipment were used. Phoenix Geophysics V8 equipment with a transmitter loop size (200 by 200 m) collected the data at 5 and 25 Hz frequencies. The Zonge TEM (300 by 300 m) transmitter loop was used to collect at 4 and 16 Hz frequencies and 10 A current. The areas around the outer caldera walls and the inner caldera were not surveyed due to challenges in accessibility.

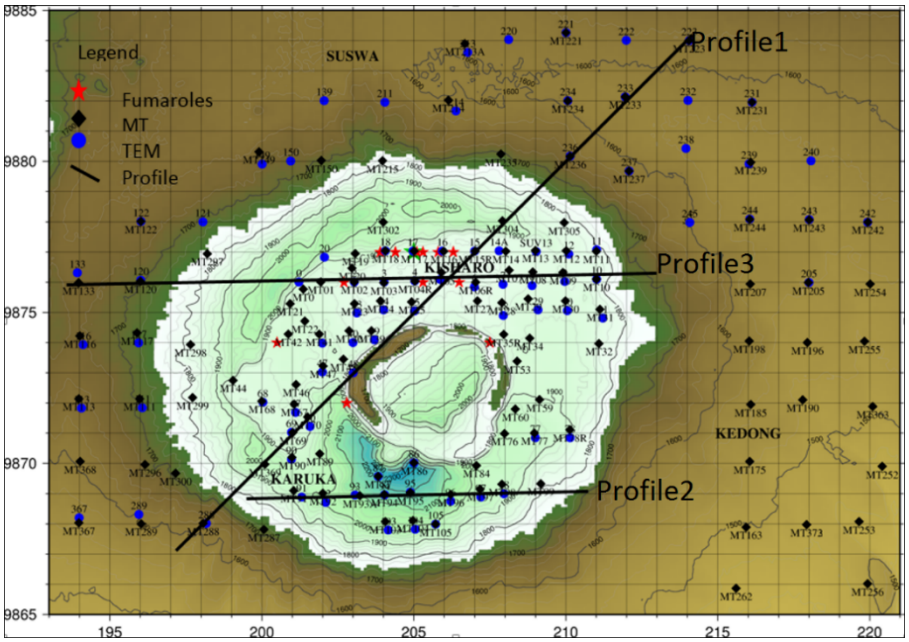

FIGURE 25: Sounding locations: Blue circles are TEM soundings, black diamonds are MT stations, red stars are fumaroles, and solid lines denote profiles

6. RESULTS OF MT AND TEM SURVEYS

The outcome of the joint 1D inversion of MT and TEM data is presented as cross-sections and iso-depth resistivity maps. Due to a large data gap between the soundings, attention should be given only to the area where the soundings are located and not the interpolated area between them for effective interpretation. Resistivity cross-sections were plotted by the TEMCROSS programme developed at ÍSOR (Eysteinsson, 1998). The program calculates the best line between the selected sites on a profile and plots resistivity iso-lines based on the 1D model generated for each sounding. It is actually the logarithm of the resistivity that is contoured so that the colour scale is exponential, but the numbers at the contour lines are resistivity values (Barkaoui, 2011).

Three cross-sections were generated down to a depth of 10,000 m b.s.l., and down to sea level (1800 m below ground surface) while iso-depth resistivity slices were generated at 1600 and 1000 m a.s.l., sea level, and 4000 and 8000 m b.s.l.

6.1 Cross-sections

The cross-sections in Figures 26, 27 and 28 (see the location in Figure 25) point to subsurface signatures common to volcanic geothermal environments. In Figure 26 a and b (profile 1) the cross- section runs SW-NE cutting the rims and outer caldera floor. A low-resistivity anomaly in the top section to the northeast is due to sedimentary deposits associated with air fall ash during the eruption of the Suswa calderas and sequential weathering and erosion from both Mt. Longonot and Suswa. At a depth of about 3000 m b.s.l., a conductor (< 10 Ωm) persists to the end of the 10 km vertical depth in this profile. This low-resistivity anomaly at depth below the sedimentary plain to the north-northeast and east of Mt. Suswa could be due to layers of sedimentary fillings in the rift since its inception. In addition to lake sediments in the rift basin, the rift is tectonically active with micro-seismic activities that continuously

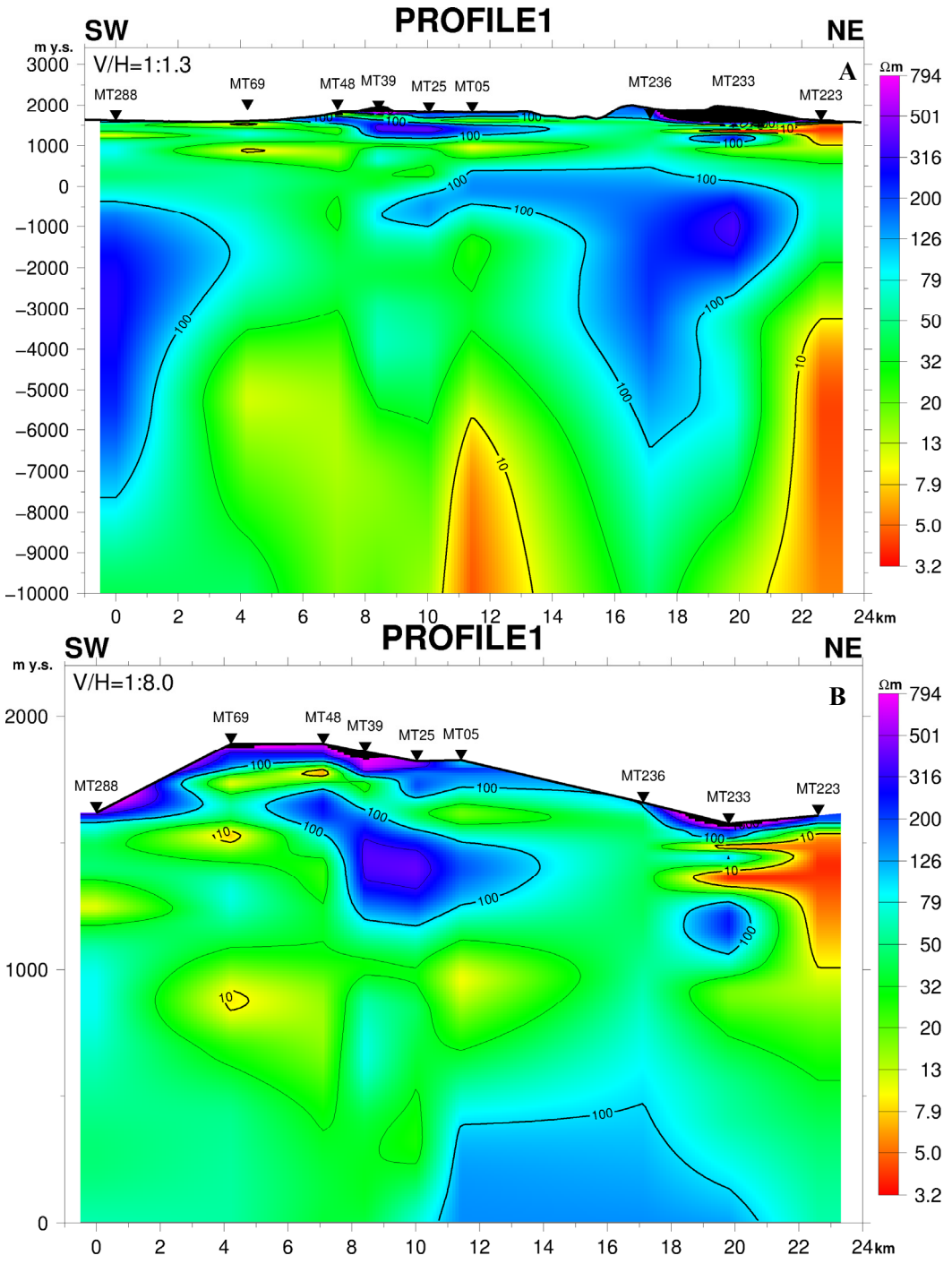

FIGURE 26: Resistivity cross-section profile 1;
a) Down to 10,000 m b.s.l.; b) Down to sea level

open up fractures enhancing permeability and porosity to the deep lying sedimentary formations. Increase in pressure and temperature with sediment depth, the highly fractured rift basin, fine lake sediments, a porous media and a high-temperature gradient from the tectonically active rift system may have influenced the low resistivity in the basin. The low-resistivity anomaly common to Kenya rift below the sedimentary basin at depth is, however, not well understood. Geothermal origins have been associated with East African rift sedimentary deposits as in the case of Tendaho in Ethiopia, which could be the case in Kenya, subject to confirmation by more geoscientific research.

Below the outer caldera floor, at about 1000 m a.s.l., a low-resistivity anomaly probably caused by low-temperature alteration minerals (zeolite/ smectite) is shown in Figure 25. Above this layer, a deep

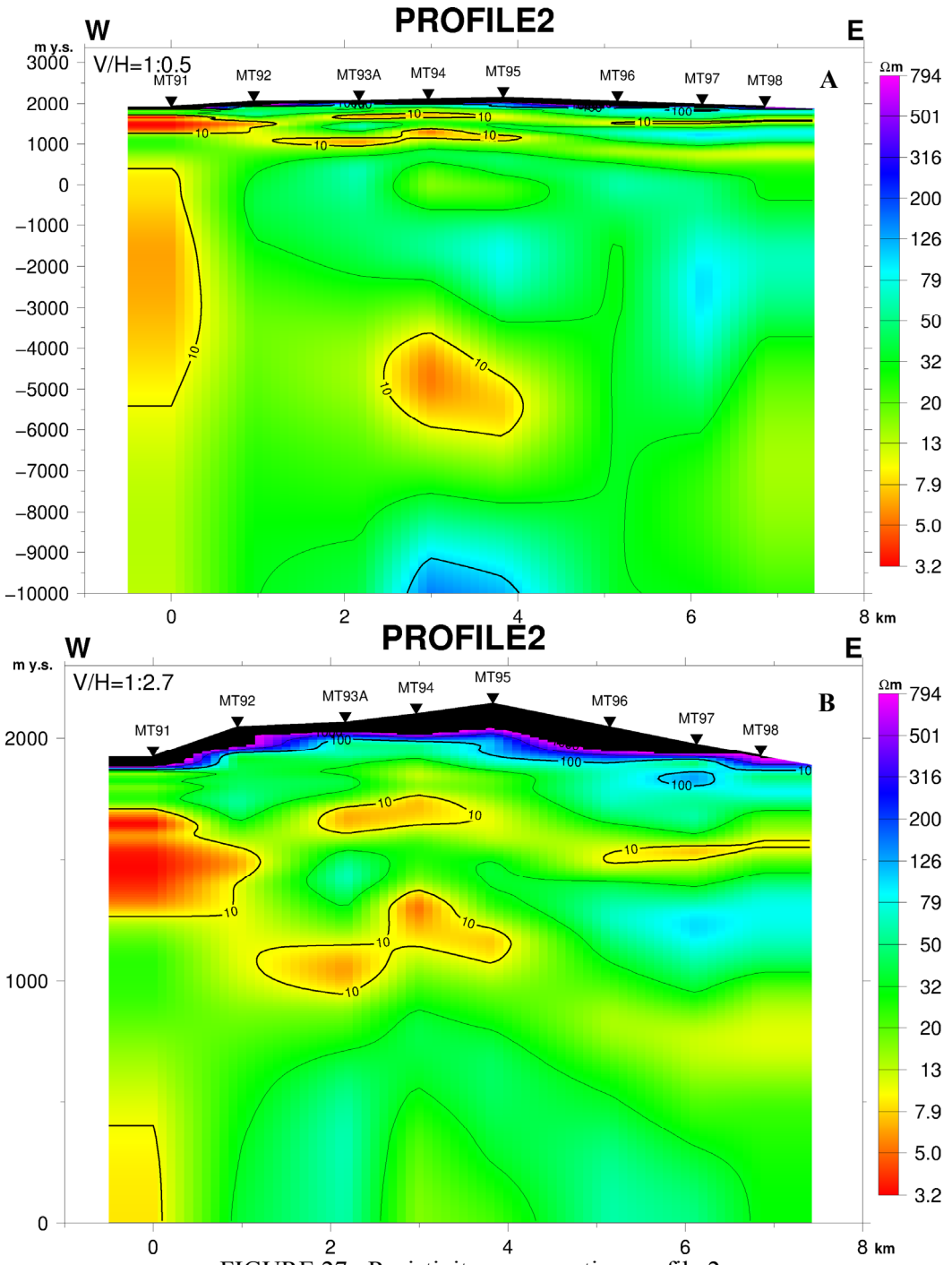

FIGURE 27: Resistivity cross-section profile 2:
a) Down to 10,000 m b.s.l.; b) Down to sea level

groundwater table could be inferred from the high resistivity. It is associated with fumaroles which are presumably due to dry steam. The near surface high resistivity is caused by remnants of unaltered rocks. High resistivity oriented vertically below the rims of the caldera clearly demarcate the caldera walls both in depth and breadth and probably the extent of the geothermal field. The resistive core at sea level (0 m) below the conductive cap (see Figure 26) is most likely caused by high-temperature alteration minerals consistent across the Suswa caldera. Below the resistive core is the deep seated doming conductor (< 10 Ωm), presumed to be connected to the heat source.

Figure 27 shows a profile across the southern slope of the outer caldera. High resistivity near the surface is unaltered formations associated with recent phonolitic lava flow from the most recent eruptions, below

which are conductive layers (about 1000 m a.s.l.), associated with volcanic ash deposits from pre-caldera eruptions and low-temperature mineral alterations. At depths between 3000 and 6500 m b.s.l., a pocket of conductive bodies is found in the centre of the profile which could be part of the heat source. At the western corner (below sounding MT91), a much closer conductor (1500 m a.s.l.) prominent near the surface and at depth between 500 m a.s.l., and 5500 m b.s.l., could probably be due to the sedimentary basin deposits discussed above.

Figure 28 shows profile 3 across the floor of the northern caldera and the western rim of the outer caldera and western slopes. The profile shows similar features as seen in profile 1 inside the caldera and profile

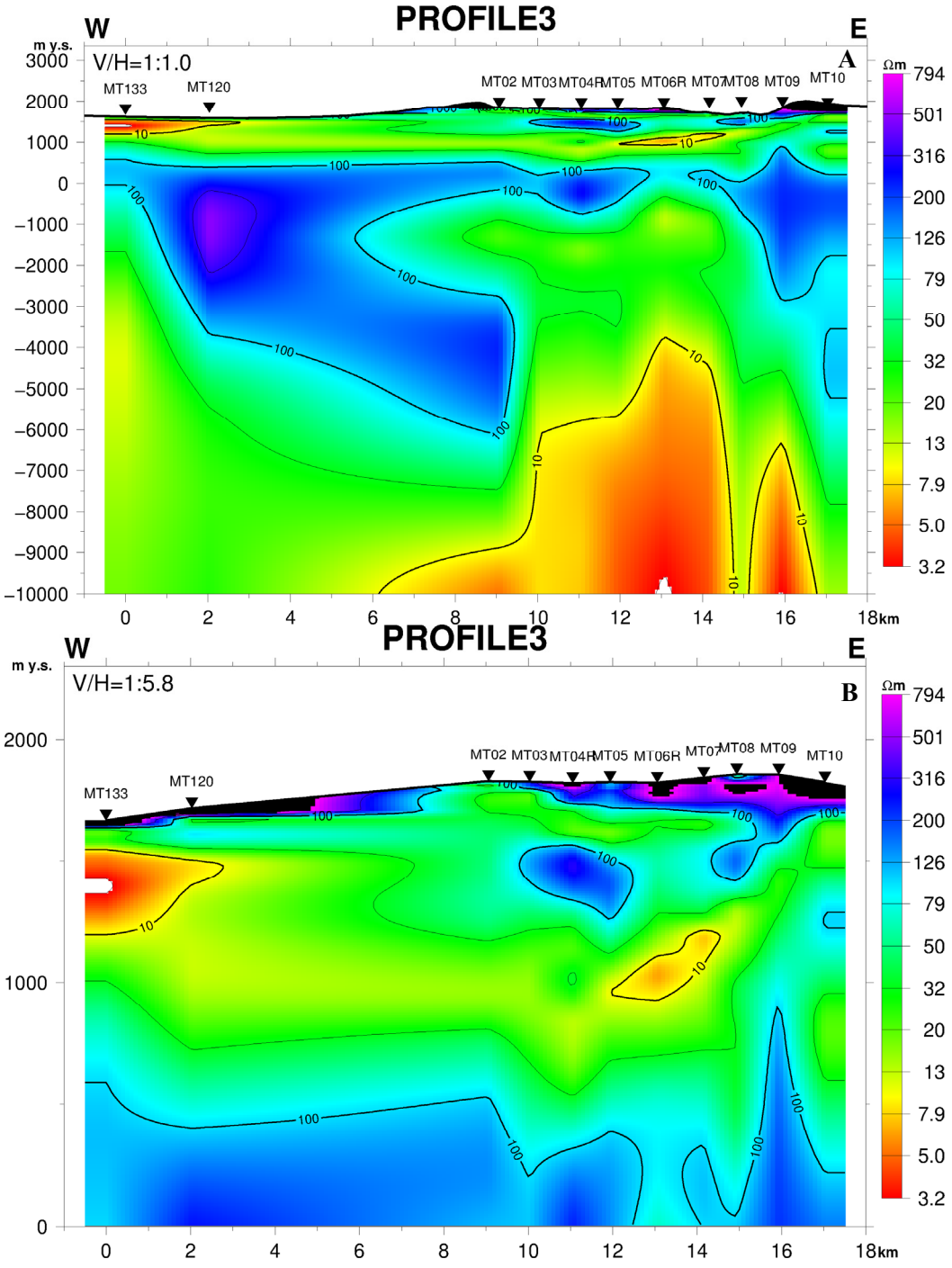

FIGURE 28: Resistivity cross-section profile 3:
a) Down to 10,000 m b.s.l.; b) Down to sea level

2 to the western side. The high-resistivity core at sea level is confined between low resistivity above 500 m a.s.l., related to low-temperature alteration minerals and a deeper conductor below 4000 m b.s.l., presumed to be the heat source. The heat plume is right below the caldera.

6.2 Iso-resistivity maps

Iso-resistivity depth maps (Figures 29-33) were generated using the *TEMRESD* programme (Eysteinsson, 1998) from 1D Occam models at different elevations, contoured and coloured in a logarithmic scale. Figure 29 is at a depth of 1600 m a.s.l., and shows a shallow conductive layer attributed to weathering, volcanic ash and sedimentary deposits to the south. The high-resistivity area below the fumarolic areas may have resulted from unaltered formation and a low level of water-rock interaction because of the high steam level in the fumaroles attributed to a deep groundwater table in Suswa. Thus, the absence of near surface geothermal fluids and dry steam causes a resistivity high in fumarolic areas in the northern floor of the outer caldera.

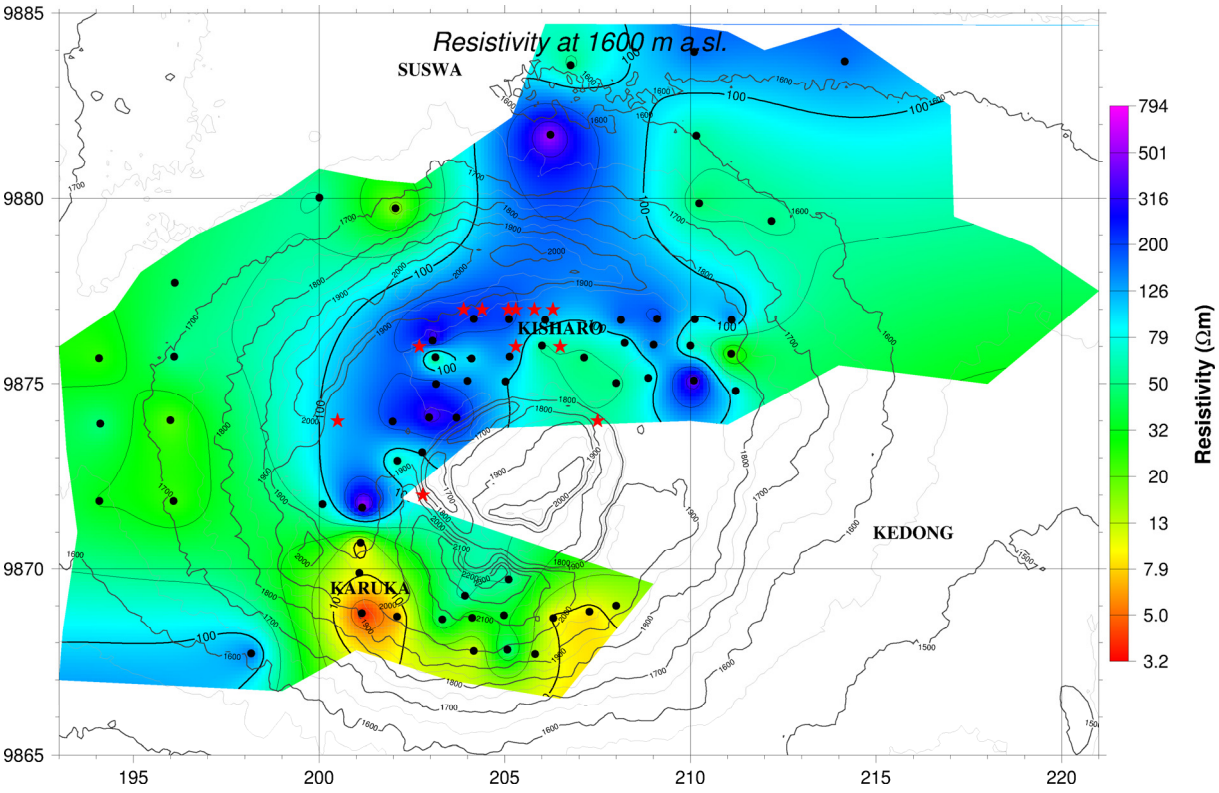

FIGURE 29: Resistivity map at 1600 m a.s.l.;
black dots denote MT soundings and red stars are fumaroles

In Figure 30, a low-resistivity anomaly is now evident at 1000 m a.s.l., which could be the result of low-temperature alteration minerals.

Figure 31 shows high resistivity at sea level (0 m), attributed to high-temperature alteration minerals common to high-temperature volcanic geothermal systems. Resistivity highs also demarcate the caldera walls at the rims and at depth. A less resistive zone bordering the inner caldera ring and oriented in a NE-SW direction could indicate a structural alignment following the caldera axis. This structure could be the main conduit of the geothermal fluid and is associated with the upflow zone of the system below the calderas.

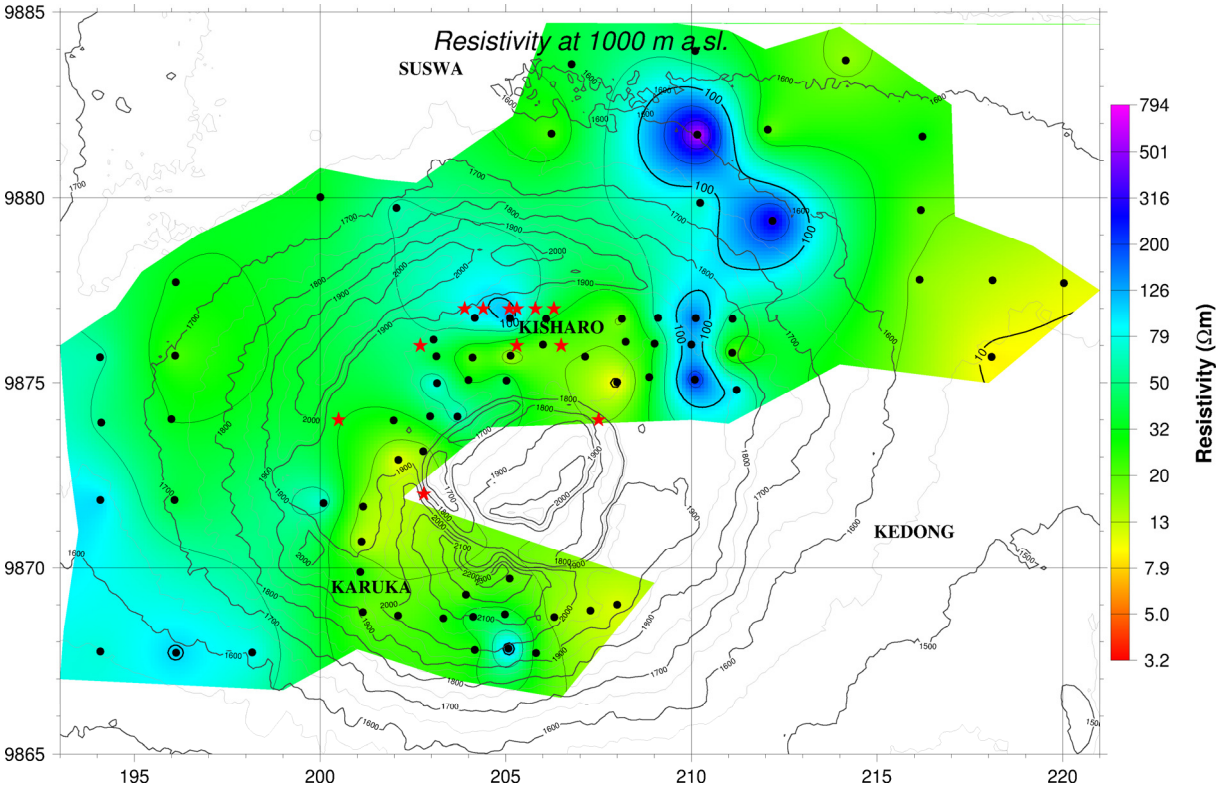

FIGURE 30: Resistivity map at 1000 m a.s.l.

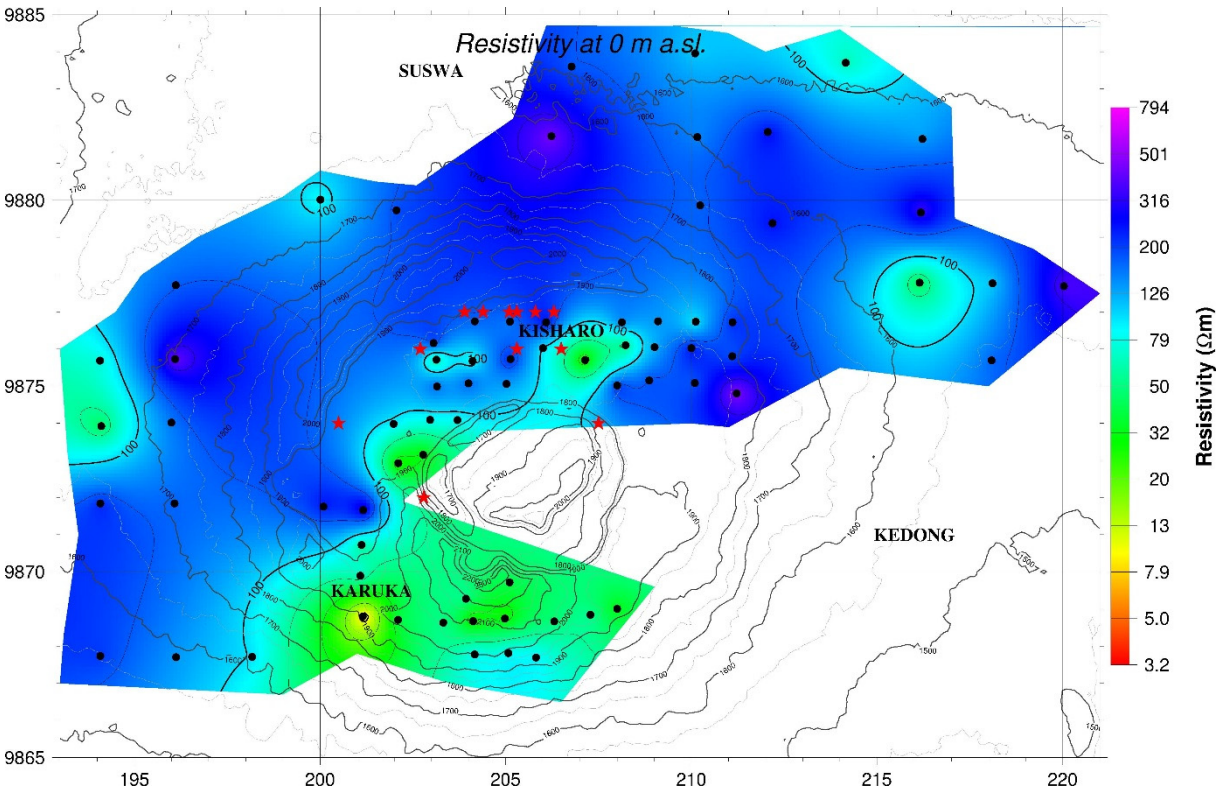

FIGURE 31: Resistivity map at sea level

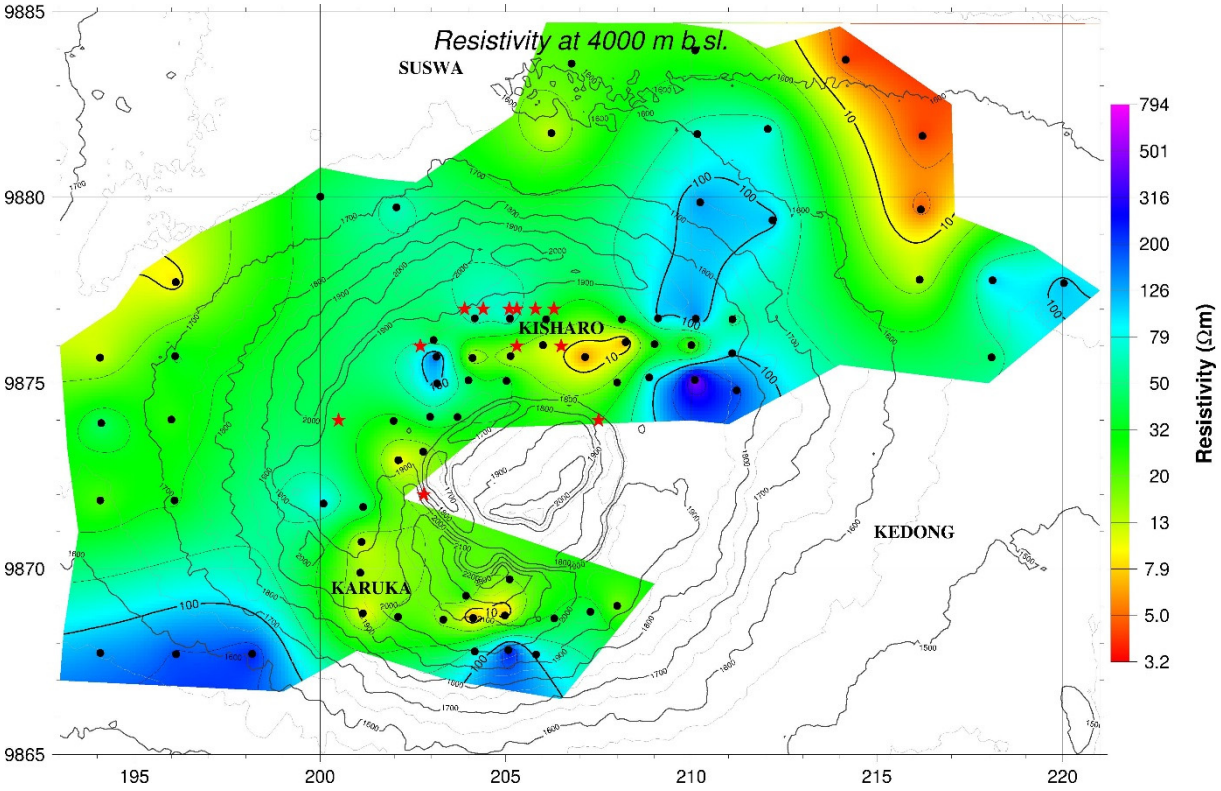

FIGURE 32: Resistivity map at 4000 m b.s.l.

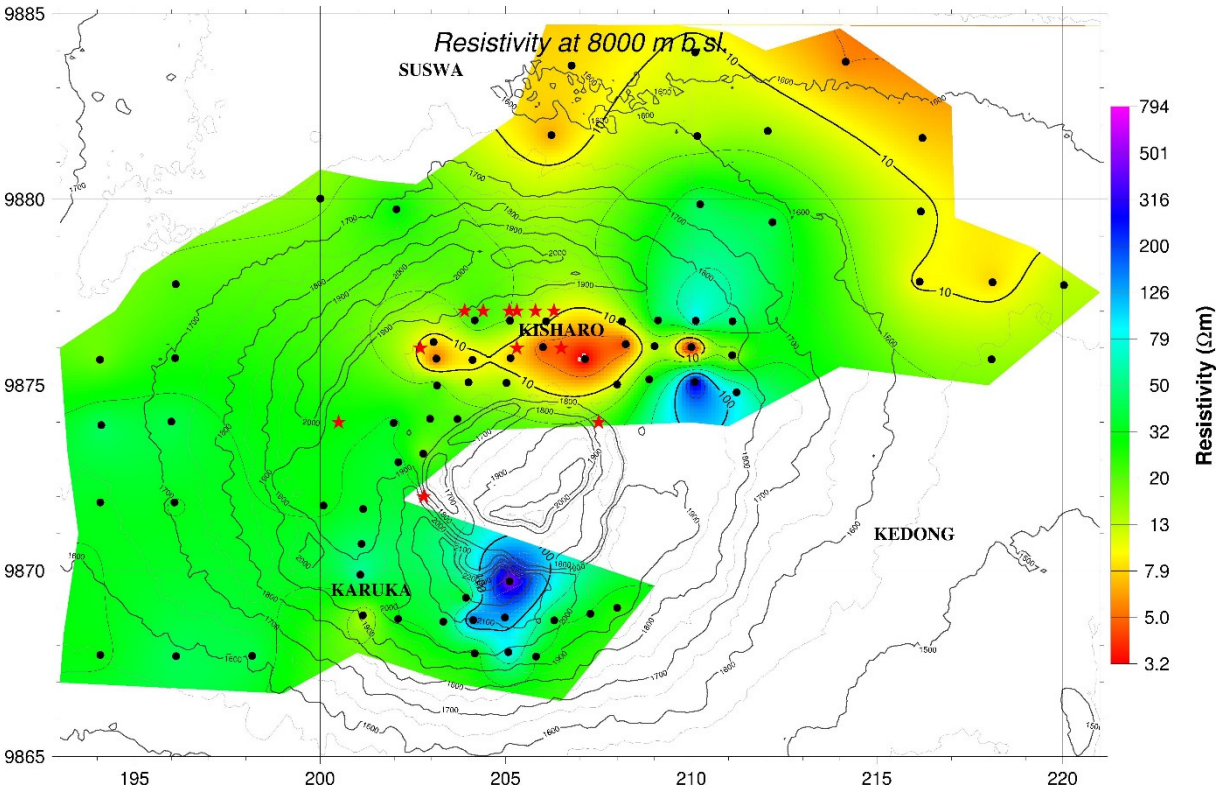

FIGURE 33: Resistivity map at 8000 m b.s.l.

Figure 32 shows the top of the deep conductors at 4000 m b.s.l, which together presumably form the heat source. These conductors are seen to the north, south and west of the inner caldera. However, there are no data in the inner caldera to establish if the heat sources are connected or discrete. The NE-SW structural alignment of conductive bodies encircling the inner caldera is obvious. It must be noted that the conductors are very pronounced, oriented along the dense fumaroles in the caldera. The low-resistivity anomaly to the northeast is outside the caldera in a sedimentary basin between Suswa, Domes and Longonot, as discuss above.

Figure 33 shows an iso-depth map at 8000 m b.s.l. showing conductive bodies (< 10 Ωm) at the floor of the outer caldera in the north, trending W-E and to the north and north-northeast of the outer caldera in the sedimentary plain. The conductive area increases with an increase in subsurface depth and seems to merge (12,000 m b.s.l. not shown in this report). The deep conductors cannot be established south and west of the caldera at depths below 6000 m b.s.l., probably due to their formation in pockets with a source below the inner caldera where the last eruption occurred. The persistence of the main conductive body below the fumaroles in the north, oriented W-E, could be the main source of heat for Suswa prospect.

7. CONCLUSIONS AND RECOMMENDATIONS

Suswa has a geothermal potential, as shown by the resistivity cross-sections and iso-depth maps and strike analysis. The classical high-low-high-low pattern common in volcanic regions with a geothermal system is displayed, i.e. surface highs due to resistivity caused by unaltered rocks, followed by low resistivity at around 1000 m a.s.l, due to low-temperature alteration minerals. At sea level (0 m) a resistive core was found, most likely associated with high-temperature alteration minerals. Deep conductors below 4000 m b.s.l. could be the heat source for the Suswa geothermal system. The independent strike analysis of induction arrows and Tipper strike based on H_z confirms resistivity structures, generated from the two electrical and magnetic components.

The low resistivity in the sedimentary basin at depth could be due to deep conductive lake sediments, porous media, and a highly fractured rift basement due to active tectonic and micro-seismic activities that permeate fluids within the rift sedimentary structures.

7.1 Recommendations

1) A resistivity survey of the inner caldera would delineate the source of the deep conductors seen in the south as pockets and would probably show if they are connected to deep conductors in the north.

2) A resistivity survey of the north-northeast and eastern sedimentary plain (Kedong Ranch) connecting Suswa to Domes and Longonot area could establish geothermal signatures to the east of Suswa town.

3) More TEM infill should be conducted for the sites where MT surveys have already been done.

4) 3D inversion of MT data for Suswa prospect would give better resolution in delineating the resource signatures.

5) Additional surface exploration work could lead to the creation of a conceptual model of the area.

ACKNOWLEDGEMENTS

I wish to acknowledge the UNU-GTP and Icelandic Government for the six month UNU Fellowship award, ÍSOR - Iceland GeoSurvey and Orkustofnun - the Icelandic National Energy Authority for their outstanding teaching staff and provision of support materials and Geothermal Development Company for providing the data and granting me a study leave.

Many thanks go to Dr. Ingvar Birgir Fridleifsson (former director), current director Mr. Lúdvík S. Georgsson, Ms. Thórhildur Ísberg, Mr. Ingimar G. Haraldsson, Ms. Málfrídur Ómarsdóttir and Mr. Markús A.G. Wilde, for their terrific support and facilitation of the training programme.

Special thanks to my supervisors, Mr. Gylfi Páll Hersir and Mr. Knútur Árnason for their assistance, availability and open door policy and advice during the study time. I wish to give my thanks to Mr. Arnar Már Vilhjálmsson and Mr. Andemariam Teklesenbet for their assistance with my project.

More thanks to colleagues at UNU-GTP in Geophysical Exploration section for their fruitful discussions and sharing of knowledge. To the entire UNU-GTP fellows of 2013, much thanks. To my colleagues at GDC geophysics section, my utmost gratitude for your support especially in data acquisition.

To my family, your support during these six months away was paramount. Most importantly, thanks to the Almighty Allah who taught mankind by the pen what they didn't know. Certainly I have learnt much in this training.

REFERENCES

Archie, G.E., 1942: The electrical resistivity log as an aid in determining some reservoir characteristics. *Tran. AIME, 146,* 54-67.

Árnason, K., 1989: *Central loop transient electromagnetic sounding over a horizontally layered earth*. Orkustofnun, Reykjavík, report OS-89032/JHD-06, 129 pp.

Árnason, K., 2006a: *TemX short manual*. ÍSOR – Iceland GeoSurvey, Reykjavík, internal report, 17 pp.

Árnason, K., 2006b: *TEMTD (Program for 1D inversion of central-loop TEM and MT data)*. ÍSOR – Iceland GeoSurvey, Reykjavík, short manual, 16 pp.

Árnason, K., 2008: *The magnetotelluric static shift problem.* ÍSOR - Iceland GeoSurvey, report ÍSOR-08088, 16 pp.

Árnason, K., Eysteinsson, H., and Hersir, G.P., 2010: Joint 1D inversion of TEM and MT data and 3D inversion of MT data in the Hengill area, SW Iceland. *Geothermics*, *39*, 13-34.

Árnason, K., Haraldsson, G.I, Johnsen, G.V., Thorbergsson, G., Hersir, G.P., Saemundsson, K., Georgsson, L.S., Rögnvaldsson, S.Th., and Snorrason, S.P., 1987: *Nesjavellir–Ölkelduháls. Surface exploration.* Orkustofnun, Reykjavík, report OS-87018/JHD-02 (in Icelandic), 112 pp.

Badilla E., D., 2011: Resistivity imaging of the Santa Maria sector and the northern zone of Las Pailas geothermal area, Costa Rica, using joint 1D inversion of TDEM and MT data. Report 8 in: *Geothermal training in Iceland 2011.* UNU-GTP, Iceland, 85-118.

Barkaoui, A.E., 2011: Joint 1D inversion of TEM and MT resistivity data with an example from the area around the Eyjafjallajökull glacier, S-Iceland. Report 9 in: *Geothermal training in Iceland 2011*. UNU-GTP, Iceland, 119-148.

Biggs, J., Anthony, E.Y., and Ebinger, C.J., 2009: Multiple inflation and deflation events at Kenyan volcanoes, East African Rift. *Geology, 37-11,* 979–982.

Cagniard, L., 1953: Basic theory of the magneto-telluric method of geophysical prospecting. *Geophysics, 18*, 605-635.

Cantini, P., Cataldi, A., and Pinna., E., 1990: Gravity study of the structure of Suswa volcano and basement in the Kenya Rift. *Geothermics, 19-4*, 367–384.

Christensen, A., Auken, E., and Sorensen, K., 2006: The transient electromagnetic method. *Groundwater Geophysics, 71,* 179-225.

Espejel-García, V., 2009: *Suswa volcano, Kenya rift: Evidence of magma mixing, Na-F complexing and eruptions triggered by recharge.* University of Texas, El Paso, PhD thesis, 115 pp.

Eysteinsson, H., 1998: *TEMMAP, TEMRESD and TEMCROSS plotting programs*. ÍSOR – Iceland GeoSurvey, Reykjavík, unpublished programs and manuals.

Flóvenz, Ó.G., Spangenberg, E., Kulenkampff, J., Árnason, K., Karlsdóttir, R., and Huenges E., 2005: The role of electrical conduction in geothermal exploration. *Proceedings of the World Geothermal Congress 2005, Antalya, Turkey,* CD, 9 pp.

Flóvenz, Ó.G., Hersir, G.P., Saemundsson, K., Ármannsson, H., and Fridriksson Th., 2012: Geothermal energy exploration techniques. In: Syigh, A., (ed.), *Comprehensive renewable energy, vol. 7*. Elsevier, Oxford, 51-95.

GDC, 2013: *Suswa geothermal prospect*. GDC, unpublished report, 107 pp.

Georgsson, L.S., and Karlsdóttir, R., 2009: Resistivity methods - DC and TEM with examples and comparison from the Reykjanes peninsula and Öxarfjördur, Iceland. *Paper presented at "Short Course on Surface Exploration for Geothermal Resources", organized by UNU-GTP and LaGeo, in Ahuachapan and Santa Tecla, El Salvador*, 14 pp.

Hersir, G.P., and Árnason, K., 2010: Resistivity methods - MT. *Paper presented at „Short Course V on Exploration for Geothermal Resources", organized by UNU-GTP, GDC and KenGen at Lake Bogoria and Lake Naivasha, Kenya,* 7 pp.

Hersir, G.P., Árnason, K and Steingrímsson, B., 2009: Exploration and development of the Hengill geothermal field. *Paper presented at "Short Course on Surface Exploration for Geothermal Resources", organized by UNU-GTP and LaGeo, in Ahuachapan and Santa Tecla, El Salvador*, 14 pp.

Hersir, G.P., Árnason, K., and Vilhjálmsson, A.M., 2013: 3D inversion of magnetotelluric (MT) resistivity data from Krýsuvík high temperature geothermal area in SW Iceland. *Proceedings of the 38th Workshop on Geothermal Reservoir Engineering, Stanford University, Stanford, Ca*, 14 pp.

Hersir, G.P., and Björnsson, A., 1991: *Geophysical exploration for geothermal resources. Principles and application.* UNU-GTP, Iceland, report 15, 94 pp.

Karingithi, C., Arnórsson, S,, and Grönvold, K., 2010: Processes controlling aquifer fluid compositions in the Olkaria geothermal system, Kenya. *J. Volcanology & Geothermal Research, 196*, 57–76.

Keller, G.V., and Frischknecht, F.C., 1966: *Electrical methods in geophysical prospecting.* Pergamon Press Ltd., Oxford, 527 pp.

Lagat, J., 2003: Geology and the geothermal systems of the southern segment of the Kenya Rift. *Proceedings of the International Geothermal Conference IGC2003 "Multiple integrated uses of geothermal resources", Reykjavik*, S12, 33-40.

McCall, G.J.H., and Bristow, C.M., 1965: An introductory account of Suswa volcano, Kenya. *Bulletin Volcanologique, 28-1*, 333-367.

McNeill, 1994: *Principle and application of time domain electromagnetic techniques for resistivity sounding.* Geonics Ltd., Ontario, technical note TN 27, 15 pp.

Mohamud, Y.N., 2013: Appendices to the report "*1D joint inversion of TEM and MT data: Suswa geothermal field, Rift Valley, Kenya*". UNU-GTP, Iceland, report 19 appendices, 92 pp.

NGA, 2013: *Geophysical methods*. Northwest Geophysical Associates, Inc., website: *www.nga.com/Geo_ser_DC_tech.htm.*

Omenda, P.A., 1997: *The geochemical evolution of Quaternary volcanism in the south central portion of the Kenya rift.* University of Texas, El Paso, PhD thesis, 217 pp.

Omenda P.A., 1998: The geology and structural controls of the Olkaria geothermal system, Kenya. *Geothermics, 27-1,* 55-74.

Omenda, P.A., 2007: Status of geothermal exploration in Kenya and future plans for its development. *Paper presented at "Short Course II on Surface Exploration for Geothermal Resources", organized by UNU-GTP and KenGen, at Lake Naivasha, Kenya*, 13 pp.

Onacha, S., Shalev, E., Malin, P., and Leary, P., 2009: Joint Geophysical Imaging of fluid-filled fracture zones in geothermal fields in the Kenyan Rift Valley. *Geother. Resource Council, Trans., 33, 465-471.*

Phoenix Geophysics, 2005: *Data processing user guide*. Phoenix Ltd., users guide.

Quist, A.S., and Marshall, W.L., 1968: Electrical conductances of aqueous sodium chloride solutions from 0 to 800°C and at pressures to 4000 bars. *J. Phys. Chem., 72,* 684-703.
Rowland, B.F., 2002: *Time-domain electromagnetic exploration*. Northwest Geophysical Associates, Inc., 6 pp.

SEG, 1991: *MT/EMAP data interchange standard*. Society of Exploration Geophysicists, 112 pp.

Simiyu, S.M., 1999: Seismic velocity applications to geothermal evaluation and exploitation, Southern Lake Naivasha. *Proceedings of the 24th Workshop on Geothermal Reservoir Engineering, Stanford University, Stanford, Ca.*, 131-139.

Simiyu, S.M., 2010: Application of micro-seismic methods to geothermal exploration: examples from the Kenya Rift. *Paper presented at Short Course V on Exploration for Geothermal Resources, organized by UNU-GTP, GDC and KenGen, at Lake Bogoria and Lake Naivasha, Kenya*, 27 pp.

Simiyu, S.M., and Keller, G.R., 1997: Integrated geophysical analysis of the East African Plateau from gravity anomalies and recent seismic studies. *Tectonophysics, 278,* 291-314.

Simiyu S.M., and Keller G.R., 2000: Seismic monitoring within the Olkaria geothermal field. *J. Volcanology & Geothermal Research, 95,* 197-208.

Tikhonov, A.N., 1950: Determination of the electrical characteristics of the deeper strata of the earth's crust. *Dokl. Akad. Nauk, USSR, 73,* 295-297 (in Russian).

Ussher G., Harvey C., Johnstone R., and Andersson E., 2000: Understanding the resistivities observed in geothermal systems. *Proceedings of the World Geothermal Congress 2000, Kyushu-Tohoku, Japan,* 1915-1920.

Vozoff, K., 1990: Magnetotellurics: principles and practice. *Proceedings of the Indian Academy of Sciences-Earth and Planetary Sciences, 99,* 441-471.

White, J.C., Espejel-García, V.V., Anthony, E.Y., and Omenda, P.A., 2012: Open system evolution of peralkaline trachyte and phonolite from the Suswa volcano, Kenya rift. *Lithos, 152-1,* 84–104.

.